Composites Part B 318 (2026) 113625

Contents lists available at ScienceDirect

Composites Part B

journal homepage: www.elsevier.com/locate/compositesb

3D strain mapping around fibre breaks using *in situ* synchrotron computed tomography and digital volume correlation

Yeajin Lee [a,*], Yentl Swolfs [b], Partha Paul [c,d], Marco Margini [e,f], Fernando Alvarez-Borges [a], Pierre Thibault [e,f], Yasuhiro Fukuhara [g], Tsuneo Takano [g], Naoki Sugiura [g], Mark N. Mavrogordato [a], Ian Sinclair [a], S. Mark Spearing [a]

[a] μ-VIS X-ray Imaging Centre, University of Southampton, United Kingdom
[b] Department of Materials Engineering, KU Leuven, Belgium
[c] Henry Royce Institute, Department of Materials, The University of Manchester, United Kingdom
[d] European Synchrotron Radiation Facility, Grenoble, France
[e] Department of Physics, University of Trieste, Italy
[f] Elettra-Sincrotrone Trieste, Italy
[g] Mitsubishi Chemical Corporation, Aichi, Japan

ARTICLE INFO

Keywords:
Carbon Fibre Reinforced Polymer Composites (CFRPs)
Synchrotron Radiation Computed Tomography
Digital Volume Correlation (DVC)
Fibre breaks
Load redistribution

ABSTRACT

Load redistribution around a single fibre break is a critical mechanism determining longitudinal tensile strength in carbon fibre-reinforced polymer (CFRP) composites, with understanding of this process historically relying on model predictions. Digital Volume Correlation (DVC) combined with high-resolution computed tomography has previously enabled the experimental quantification of strains around fibre breaks, using volumetric speckle patterns generated by the addition of fiducial particles to the composite matrix. Applying fiducial particles to CFRP to interrogate the length scales of single fibre breaks is non-trivial, as micrometre-scale inhomogeneity and particle agglomeration may compromise the broader applicability of the results. The present study extends the potential applicability of DVC, in combination with synchrotron computed tomography, by incorporating silicon dioxide (SiO_2) particles into CFRPs as a practical and improved alternative to barium titanate ($BaTiO_3$) particles used in previous work. The applicability is assessed in terms of particle distribution, DVC measurement uncertainty, and strain recovery lengths around single fibre breaks. The assessments reveal that SiO_2 particles can produce a reasonably uniformly dispersed speckle patterns with minimal apparent agglomeration, providing the fidelity required for accurate DVC measurements. On this basis, DVC strain mapping around breaks is further applied to two CFRPs with differing interfacial shear strength levels (by ~17%). DVC results indicated that the strain recovery lengths were insensitive to this change in interfacial strength, which was rationalised by the absence of detectable debonds. Overall, this study provides novel insights into load redistribution under varying interfacial strengths, offering an experimental basis for advancing longitudinal tensile strength models.

1. Introduction

Carbon fibre-reinforced polymer composites (CFRP) are widely used in structural applications across many industrial sectors, such as automotive, aerospace, construction, and renewable energy. However, failure prediction in CFRP composites remains a significant engineering challenge, complicated by their anisotropic, heterogeneous, multiscale, and intrinsically brittle nature. Predicting how initial damage evolves into final failure is particularly challenging in multidirectional composites [1]. It is widely recognised that, under tensile loads, final failure of multidirectional composites coincides with the failure of fibres oriented in the loading direction [2]. As such, understanding longitudinal tensile failure in 0° plies of unidirectional (UD) composites is essential for reliably predicting final failure.

Initial failure of CFRP within 0° plies under longitudinal tension is commonly identified to begin with the weakest fibres failing first, in accordance with some Weibull strength distribution [3–5]. As a given fibre breaks and locally loses its load-bearing capacity, load is

* Corresponding author.
E-mail address: yeajin.lee@soton.ac.uk (Y. Lee).

https://doi.org/10.1016/j.compositesb.2026.113625
Received 4 December 2025; Received in revised form 12 March 2026; Accepted 17 March 2026
Available online 18 March 2026

redistributed to neighbouring fibres via shear-dominated loading of the surrounding matrix. This shear transfer also redistributes load back onto the broken fibre, which gradually recovers stress over a characteristic distance away from the break, known as the ineffective length. Load redistribution imposes stress concentrations on neighbouring fibres over a length scale comparable to the ineffective length, thereby increasing their failure probability. As a result, additional breaks may emerge in these neighbouring fibres, creating localised break clusters [6,7]. As the load increases, some clusters grow until a critical cluster size is reached, triggering unstable propagation leading to failure [8]. Accurately quantifying the extent of load redistribution near breaks is therefore central to understand fibre break development and final failure.

Building on Cox's early shear-lag model (SLM) [9], load redistribution around single fibre breaks has been extensively investigated by both SLMs [10–13] and finite element (FE) methods [14–19]. Two key parameters for characterising load redistribution are the ineffective length of the broken fibre and the stress concentration factors in the neighbouring intact fibres [20], both being strongly influenced by modelling assumptions. Recent 3D FE modelling by AhmadvashAghbash et al. [21], for instance, offers detailed predictions of load redistribution around a single fibre break by accounting for interfacial debonding. Their model addressed UD composites with random fibre packing, incorporating key physical contributors to debonding, including interfacial shear strength, thermal residual stresses, matrix plasticity, and matrix cracking. In particular, their results demonstrated that higher interfacial strength, toughness, and high thermal residual stresses restrained debond propagation, which then increased stress concentration on neighbouring fibres. Conversely, increased debond lengths combined with more matrix plasticity were found to reduce and delocalise stress concentrations, distributing them over longer fibre lengths. While such models provide valuable insight into failure, experimental validation remains essential to substantiate changes in load redistribution behaviour that may or may not arise from changing interfacial strengths.

Experimental approaches to monitor load redistribution at fibre breaks have been employed using 2D surface measurement techniques, such as Raman spectroscopy [22–24] and *in situ* microscopy combined with Digital Image Correlation [25,26]. These methods, however, are limited in their ability to represent the highly constrained and 3D stress/strain states associated with microscale damage occurring within the actual bulk material. Advances in X-ray Computed Tomography, particularly Synchrotron Radiation Computed Tomography (SRCT), have enabled 3D, *in situ* imaging of composites at a resolution sufficient to distinguish individual fibre breaks [6,27–31] and their development under increasing load. Scott et al. [32] indirectly estimated ineffective length from SRCT volumes by measuring the spacing between two successive breaks along the same carbon fibre. As such, they reported an ineffective length of ~70 μm, notably smaller than most analytical and numerical predictions [33].

Digital Volume Correlation (DVC) coupled with *in situ* CT volumes has emerged as a non-intrusive experimental technique, enabling full-field quantification of local displacements and strains within materials at different load states [34–37]. DVC, a 3D extension of Digital Image Correlation, determines local displacement fields by correlating local greyscale patterns between consecutive CT volumes. For reliable correlation, these features should provide a uniform stochastic distribution, and possess sufficient contrast to be trackable between consecutive CT volumes. DVC has been applied to composites by exploiting their fibrous texture as trackable patterns under favourable conditions [38–44]. However, this becomes intrinsically challenging for unidirectional CFRPs at small length-scales, as the fibre distributions are highly self-similar and indistinguishable along the fibre direction. Under these conditions, correlation accuracy is severely compromised, underscoring the need for artificial volumetric speckle patterns (i.e. fiducial markers).

Brault et al. [45] have demonstrated the use of relatively large copper particles (150 μm) between UD carbon fibre plies as volumetric speckle patterns to enable DVC to map transverse shear strains. More recently, several studies [46–51] have extended this approach to the intralaminar material by dispersing sub-micrometre particles such as barium titanate ($BaTiO_3$, 400 nm) and titanium carbide (TiC, 800 nm) within the matrix itself, enabling DVC measurements within the fibre plies. Schöberl et al. [47] first demonstrated DVC strain measurements at the individual fibre level by combining $BaTiO_3$-doped CFRPs with *in situ* SRCT (650 nm voxel size). These measurements mapped local longitudinal strains around single fibre breaks along the fibre direction, revealing an ineffective length of ~37 μm on each side of the break plane. While an extensive trial of alternative materials was used to optimise particle distributions, this study remained limited by a degree of particle clustering, thereby creating particle-sparse regions (compromising correlation accuracy) and particle-rich regions (compromising the local fibre distribution and alignment). This behaviour is consistent with the intrinsic tendency of particles to aggregate due to high surface energy and large surface area [52]. Moreover, $BaTiO_3$ particles are not a typical polymer filler, limiting the broader applicability of this approach in polymer composites.

Accordingly, it is desirable to identify alternative materials that may provide comparable or improved DVC performance to $BaTiO_3$ particles, while reducing susceptibility to inhomogeneity and agglomeration. To this end, the present study introduces industrial-grade silicon dioxide particles (SiO_2), with a nominal particle diameter of 500 nm, as a practical alternative for generating volumetric speckle patterns, with the choice informed by two attributes. First, SiO_2 particles are widely used as a functional filler in polymer composites, indicating their good compatibility with polymers [53]. Second, SiO_2 particles tend to disperse more uniformly with reduced agglomeration, attributable to their lower surface energy, density closer to the epoxy, and stronger electrostatic repulsion [54]. However, SiO_2 with its lower atomic number constituents, exhibits lower X-ray attenuation than $BaTiO_3$ particles, reducing image contrast and potentially compromising efficacy as a fiducial marker.

On this basis, this study explores the efficacy of DVC in SiO_2-doped CFRPs under *in situ* SRCT tensile testing. This is discussed in three aspects: (1) particle distribution, (2) DVC measurement uncertainty, and (3) ineffective length measurements (i.e. hereafter referred to as the 'strain recovery length', see Section 4.3.1). In addition, we investigate two CFRPs produced with different fibre surface treatments, resulting in different interfacial shear strengths, and measure the corresponding strain recovery lengths around fibre breaks via DVC. Experimental demonstration of how interfacial shear strength influences load redistribution around fibre breaks has not previously been reported via such full-field strain mapping. Finally, the DVC-estimated recovery lengths are interpreted in relation to the associated damage mechanisms and previously reported analytical and numerical estimates.

2. Materials and methods

2.1. Materials

$[90_2/0_2]_s$ cross-ply laminates of carbon fibre/epoxy prepreg were provided by Mitsubishi Chemical Corporation, with a total thickness of ≈1 mm. Two prepregs were produced using the same MRZ65-18000 carbon fibres with a #350 series amine-curing epoxy (Mitsubishi Chemical Corporation), distinguished only by fibre surface treatments designed to yield lower and higher interfacial shear strengths (i.e. stronger adhesion to the matrix-fibre interfaces), respectively. For simplicity, the prepregs produced with the two surface treatments are hereafter referred to as low- and high-interfacial strength materials. Tables 1 and 2 summarise the fibre properties corresponding to the two surface treatments and the #350 series epoxy resin used in the low and high interfacial strength materials, respectively. Table 3 presents the Weibull parameters and interfacial characteristics derived from single fibre tensile and fragmentation tests. The average tensile strength at

Table 1
Physical and mechanical properties of carbon fibres with low and high interfacial strengths.

Material type	Low interfacial strength	High interfacial strength
Number of filaments	18000	18000
Nominal fibre diameter, d_f [μm]	5.58	5.58
Yield [mg/m]	796	800
Density [g/cm^3]	1.815	1.814
Tensile (strand) strength [GPa]	6.40	6.36
Tensile (strand) modulus [GPa]	286	287

Table 2
Physical and mechanical properties of the #350 series epoxy resin.

Material type	#350 series epoxy
Density [g/cm^3]	1.21
Tensile (strand) modulus [GPa]	3.73
Shear modulus [GPa]	1.29
Poisson's ratio	0.411
Yield stress [MPa]	89
Coefficient of Thermal expansion at 23 °C [10^{-6}/°C]	53.1

critical fibre length ($\sigma_f(l_c)$) and interfacial shear strength (τ) were determined using the following eqs. (1) and (2):

$$\sigma_f(l_c) = \sigma_0 l_c^{-1/m} \Gamma\left(1 + {}^1\!/_m\right) \tag{1}$$

$$\tau = \frac{\sigma_f(l_c)\, d_f}{2 l_c} \tag{2}$$

where σ_f is the fibre strength, l_c the critical fibre length, σ_0 the Weibull scale parameter for the flaw distribution, m the Weibull modulus or shape parameter for the flaw distribution, and d_f the nominal fibre diameter. It should be noted that the single fibre fragmentation tests (SFFTs) were performed using a model epoxy resin (jER 828), not the matrix resin of the low and high interfacial strength materials. This was necessary, as the epoxy used in the prepreg was not available as a neat resin. Consequently, the measured values confirm relative differences in interfacial shear strength but may not represent their absolute values in the actual prepreg matrix.

The matrix material was doped with silicon dioxide particles (SiO_2) with a nominal diameter of ~500 nm and a near-spherical shape. Fig. 1 presents representative SRCT images, highlighting the contrast associated with the resulting speckle patterns and microstructural differences compared with undoped CFRPs. The concentration of SiO_2 particles was set to ~10 wt% of the resin, equivalent to 2.3 vol%. This combination of particle attributes was selected to minimise impact on the mechanical behaviour of the polymer matrix system, as suggested in Refs. [46,49]. As such, a comparison of the macroscopic tensile strength of neat and particle-doped materials is provided in section 2.2. The prepreg laminates were cured in an autoclave under standard aerospace-grade processing conditions, except that the curing temperature was set to 130 °C.

2.2. Specimen design

Double-notched specimens, with a nominal notch section width of 1 mm between the notch roots, were prepared for *in situ* tensile testing. Fig. 2b and **c** illustrate the specimen geometries used. The volume fraction of 0° fibres in the notch region, as measured from the 3D reconstructed volume, was approximately 50%. This value was obtained by segmenting 0° fibres using the *interactive thresholding* tool in Avizo software. However, the presence of SiO_2 particles in the matrix hindered reliable fibre segmentation when attempting to segment the entire 0° fibres within the scan volume. Accordingly, a small CT sub-volume (585 μm × 455 μm × 195 μm) was cropped from the region containing 0° fibres, denoised using a *non-local means* filter in Avizo, and subsequently processed for fibre volume fraction (FVF) measurement. This procedure was repeated for eight different sub-volumes, yielding an average FVF of ~50%. The introduction of notches enabled the confinement of damage development within a small volume scanned by SRCT, allowing damage to be monitored up to near final failure. Specimens were machined via water-jet cutting, a method used previously for machining similar specimens without causing significant damage [55]. 1.5 mm thick aluminium T-tabs were attached to both ends of each specimen using aerospace adhesive, Scotch-Weld™ EC-9323 B/A (3 M Company, Maplewood, MN, USA), to aid loading and mitigate stress concentrations at the specimen ends [56].

Prior to *in situ* imaging experiments at the ID19 beamline (see section 2.3), five specimens of each material type were tested *ex situ* to determine the ultimate tensile strength (UTS) specific to the notch region. Previous testing of equivalent cross-ply specimens has shown that the 90° plies delaminate from the 0° plies at ~70% UTS and do not influence failure development in the 0° plies thereafter. Since the longitudinal tensile failure of both specimens was expected to be primarily determined by the 0° plies, only their cross-sectional area was considered in calculating the UTS. Table 4 presents the average UTS values of the neat (i.e. particle-undoped) and SiO2-doped specimens. The UTS of the SiO2-doped specimens with low and high interfacial strengths served as reference values for calculating the stepwise loads applied during *in situ* testing. The corresponding neat specimens exhibited UTS values nearly identical to those of their SiO2-doped counterparts. Two-tailed t tests were additionally performed for the neat and SiO2-doped specimens with low and high interfacial strengths, resulting in p-values of 0.76 and 0.49, respectively. These p-values, well above 0.05, indicate that particle inclusion did not significantly alter the strength of the materials.

Table 3
Weibull parameters and interfacial characteristics of CF-epoxy with low and high interfacial strengths.

Test method	Single Fibre Tensile Test	
Material type	Low interfacial strength	High interfacial strength
Weibull modulus or shape parameter, m	6.7	
Weibull scale parameter, σ_0 [GPa]	10.9	

Test method	**Single Fibre Fragmentation Test**	
Matrix type	jER 828 (epoxy resin) + *m*-Phenylenediamine (hardener)	
Material type	Low interfacial strength	High interfacial strength
Critical fibre length, l_c [mm]	0.65	0.57
Average Tensile Strength ± Standard Deviation at l_c, σ_f (l_c) [GPa]	10.8 ± 0.1	11.0 ± 0.2
Interfacial shear strength ± Standard Deviation, τ [MPa]	45 ± 4	52 ± 5

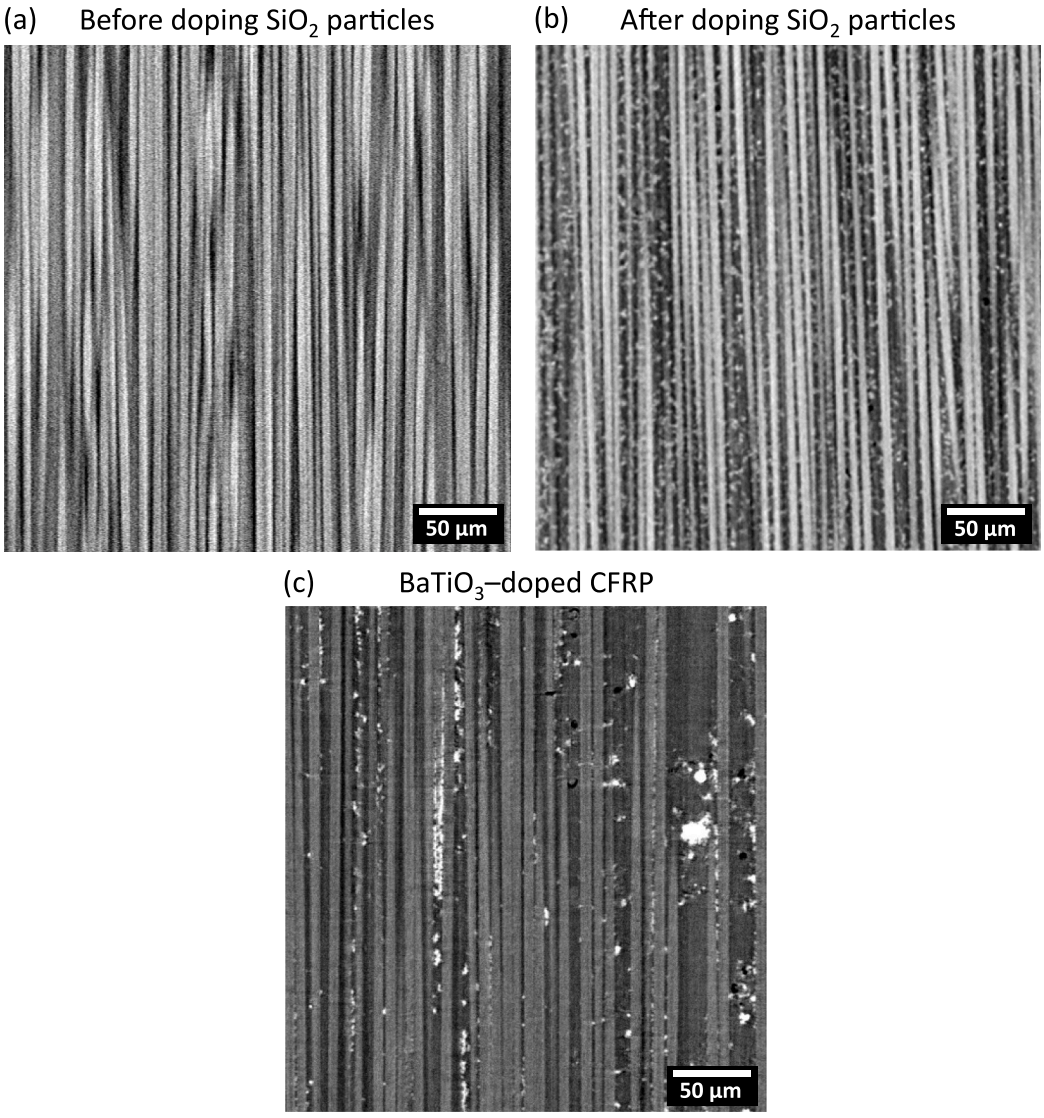

Fig. 1. SRCT images of unidirectional carbon fibre composites (a) without SiO_2 particles, showing self-similar and featureless fibre surfaces along the fibre direction, (b) with SiO_2 particles, and (c) $BaTiO_3$-doped CFRPs scanned at a 650 nm voxel size, based on data from Schöberl et al. [47].

2.3. Synchrotron Radiation Computed Tomography

In situ SRCT experiments were undertaken at 650 nm voxel size on the ID19 beamline of the European Synchrotron Radiation Facility (ESRF), Grenoble, France. A modified Deben CT5000 single-actuator electromechanical loading rig was used for *in situ* tensile testing, operating at a 0.2 mm/min displacement rate. A more detailed description of the *in situ* tensile testing apparatus is provided in Ref. [28]. A 2560 × 2160 pixel^2 detector (PCO Edge 5.5 CLHS sCMOS), positioned 50 mm from the specimen, was coupled with a LuAG:Ce single-crystal scintillator and a 10× magnification optic to achieve an effective pixel size of 650 nm, resulting in a field-of-view (FOV) of ≈1.66 × 1.40 mm^2. A "pink" beam was used to illuminate the specimen, with a peak energy set to 29 keV. A total of 1800 projections were acquired over a 180° specimen rotation with an exposure time of 100 ms per projection, resulting in a scan time of less than 5 min. Tomographic reconstruction was performed using the in-house developed reconstruction software (Nabu/Tomwer) at ESRF [57], employing a filtered back projection method, with a weak Paganin's filter [58] applied to enhance the phase contrast.

Fig. 3a illustrates schematically the sequence of loading, unloading, and reloading applied to tensile specimens. Four approximately similar incremental levels of the measured UTS were applied to specimens from low and high interfacial strength materials, corresponding to (7%, 89%, 94%, 99%) and (7%, 87%, 92%, 97%), respectively. Specimens were loaded to the first three incremental load levels (steps 1-3), with the applied load reduced by ~10% from the previous peak load prior to scanning the central notched region. This was done to mitigate potential relaxation effects during scan acquisition, while ensuring cracks remained open to aid detection.

To assess potential DVC uncertainties and obtain the DVC reference volume, simple repeat scans were carried out under both static and rigid body displacement (RBD) conditions at step 1, where the load was maintained at the lowest/preload level of 7% of UTS (i.e., the specimen being mechanically stable for scanning, but otherwise experiencing no significant damage). After scan acquisition at step 3, specimens were unloaded (step 1′) and reloaded to the same load levels as before unloading (steps 2′-3′) and one higher level (step 4′), with scans acquired at each position. Fig. 3b shows an example CT image of the introduced discontinuities, where a previously opened fibre break appears in a closed form. The scans at step 1′ onward were used to investigate the effects of discontinuities (*i.e.* the broken fibre ends and any associated imaging artefacts) on DVC performance.

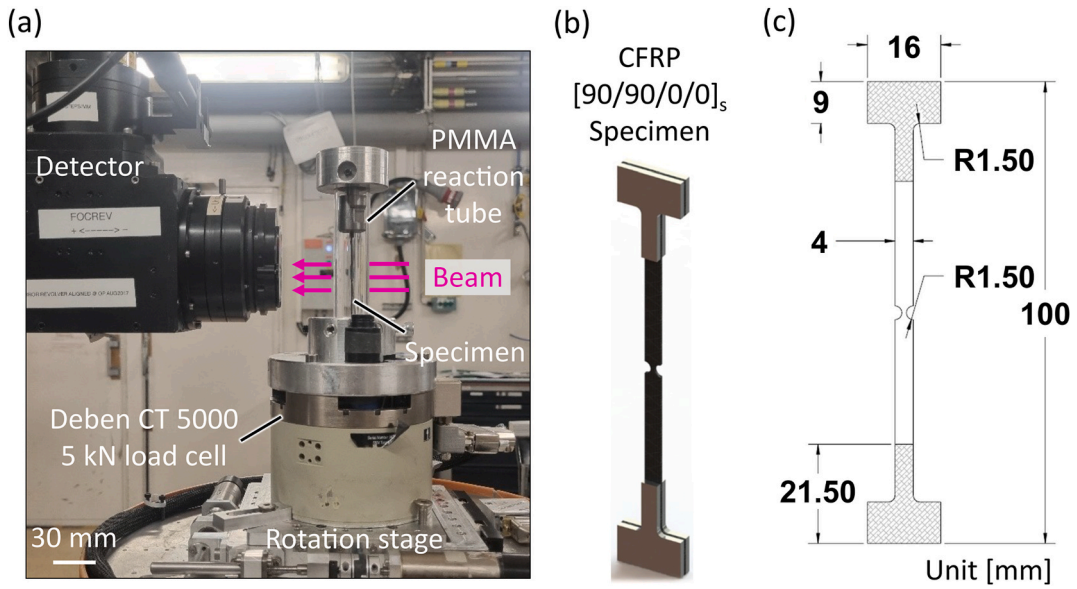

Fig. 2. *In situ* experimental setup used for 650 nm scans at the ESRF ID19 beamline: (a) *In situ* loading rig (Deben CT5000) mounted on the rotation stage, with the X-ray beam penetrating the CFRP specimen enclosed within a PMMA reaction tube, (b) Magnified view of the double-edge notched CFRP specimen with T-tabs attached to both ends [47], and (c) 2D drawing of the specimen geometry [47].

Table 4
Summary of the average ultimate tensile strength values for the neat and SiO2-doped specimens with low and high interfacial strengths, along with the p-values from a two-tailed *t*-test.

Material type	Low interfacial strength		High interfacial strength	
	Neat	SiO_2-doped	Neat	SiO_2-doped
Number of test specimens	5		5	
Average UTS ± SD [MPa]	3188 ± 123	3113 ± 128	3046 ± 226	3008 ± 60
P-value (two-tailed)	0.76		0.49	

2.4. Qualitative assessment and visualisation of particle distribution

Volumetric speckle patterns are among the key factors influencing DVC measurements of displacement and strain. Accordingly, a multi-scale qualitative approach was used to assess the distribution of sub-micrometre SiO_2 particles in the epoxy matrix in the 3D reconstructed volume using ImageJ [59,60] and Avizo 2023 software. First, the 3D reconstructed volume of the SiO_2-doped CFRP was qualitatively assessed against the distribution of speckle patterns generated with $BaTiO_3$ particles as reported by Schöberl et al. [47], both acquired at a 650 nm voxel size. Herein, CT datasets of $BaTiO_3$-doped CFRP provided by Schöberl et al. were used as a reference for the qualitative comparison.

To complement these qualitative observations, further qualitative approaches were conducted by 3D visualisation of particle distribution within a DVC sub-volume using image segmentation. Visualising particle distribution ideally requires segmenting particle features from the reconstructed volume, a process that highly depends on the image quality (*e.g.* signal-to-noise and contrast-to-noise ratios). However, the reconstructed volume, limited by a 650 nm resolution and associated imaging noise, remains insufficient to provide distinct greyscale contrast between SiO_2 particles and carbon fibres, posing challenges for particle segmentation using greyscale thresholding. To facilitate particle segmentation, we used an independent scan volume acquired via Near-Field Ptychography (NFP) at 150 nm voxel size on the same SiO_2-doped material. NFP, an X-ray phase contrast imaging technique, retrieves multiple diffraction patterns at a fixed sample-to-detector distance, while varying the transverse positions of the sample. The use of NFP, combined with tomography and a fourfold resolution improvement over 650 nm, enables the acquisition of high-resolution quantitative volumetric datasets. A detailed description of the NFP technique can be found in Refs. [61,62], while the scan acquisition and reconstruction procedure are described in Ref. [63]. The analysed SRCT NFP volumes were acquired on the ID16A beamline at the ESRF.

Fig. 4a and **b** illustrate the image processing procedure used to visualise particle distribution and agglomeration in the SRCT NFP volume, including representative processed 3D volumes and corresponding CT slices extracted from those volumes at each step. As the initial step, to assess statistical reliability, 10 distinct regions of interest were prepared at random locations by cropping from the reconstructed volume, each with a size matching the DVC sub-volume ($21 \times 21 \times 21$ μm^3). An example analysed volume is shown in Step 1 of Fig. 4a and **b**, highlighting undamaged fibres and SiO_2 particles in orthogonal 3D views and representative 2D slices (XZ and XY planes). Despite improved feature detectability in the NFP data, greyscale overlap between particles and fibres persisted, hindering exact particle segmentation. To address this, fibre features were artificially removed using ImageJ software (Step 2). A stack of 70 XZ slices, representing half of the analysed volume, was created and projected along the Y-axis (i.e. along the fibre direction) using the average intensity Z-projection function in ImageJ. Since fibres have higher greyscale intensities than other features, the average (AVG) projection resulted in a single slice containing only fibre features. As the fibres were well aligned with the Y-axis across the 70-slice stack, the perimeters of the fibre features in the AVG-projected slice closely matched those of the fibres throughout the 70 XZ slices. The AVG-projected slice was then subtracted from each of the 70 XZ slices in the stack, thereby removing the fibres. The fibre removal procedure was repeated for the remaining 70 XZ slices in the original analysed volume, and the resulting stack was concatenated with the previously processed stack.

A new stack of 140 XZ slices, containing only particles and matrix, was subsequently denoised using a *non-local means* filter in Avizo software (Step 3). This effectively reduced noise in the matrix region while preserving the well-defined edges of the particles. The filtering parameters were set to a search window of 10 pixels and a local neighbourhood of 3 pixels [38,49]. The particles were segmented using the *interactive thresholding* tool in Avizo software (Step 4). Segmentation accuracy was

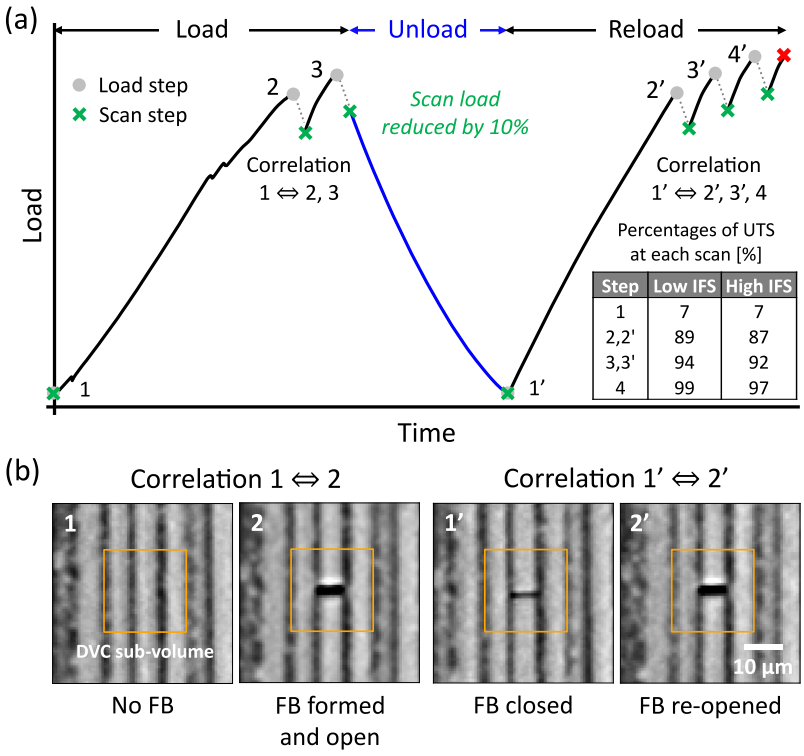

Fig. 3. (a) Schematic of the sequence of *in situ* loading (steps 1-3), unloading (steps 3-1′), and reloading (steps 1′-4′) applied to the specimens. Grey dots indicate the load levels reached at each step, and the corresponding UTS percentages for low and high interfacial strength (IFS) materials are listed in the inset table. Green 'X' marks the scan steps acquired at loads reduced by 10% from the applied levels. Red 'X' marks the final failure. Scans at step 1 and 1′ served as DVC reference volumes for the loading and reloading phases, respectively. **(b)** CT images illustrating one of DVC sub-volume regions (orange square) used to correlate a single fibre break (FB). 'FB formed and open' (step 2) indicates the formation of the fibre break, at a lower load, and the opening of a gap between the two break ends. 'FB closed' (step 1′) and 'FB re-opened' (step 2′) indicate the gap closing and reopening, resulting from the unloading and reloading. The closed fibre gap (step 1′) shows the discontinuity introduced into the DVC reference volume. (For interpretation of the references to color in this figure legend, the reader is referred to the Web version of this article.)

qualitatively assessed by overlaying the segmented particles onto CT slices of the analysed volume using the *color wash* module, allowing direct comparison. Fig. 4c presents a representative 3D visualisation of the segmented particles obtained from one of the ten analysed volumes.

2.5. Analytical prediction of recovery lengths

Although not intended for an exact validation, analytical predictions of strain recovery lengths were obtained using existing shear-lag models to assess the physical plausibility of the DVC-estimated strain recovery lengths. Herein, we employed the modified Cox's shear-lag model proposed by Landis and McMeeking [64], which additionally incorporates a shear sliding (*i.e.* interfacial slip) condition by limiting the interfacial shear stress (τ) to a prescribed shear-sliding resistance value (τ_0). While the classical Cox model assumes perfectly bonded fibre-matrix interface, this modification allows sliding once the interfacial shear stress reaches τ_0. Accordingly, interfacial sliding occurs from the break over the slip length (L_s), where the interfacial shear stress remains constant at τ_0. Beyond this slip region, the matrix is assumed to resume load transfer elastically, allowing the stress in the broken fibre to recover progressively toward the far-field applied stress. Further analytical background and derivation details of this modified Cox's model can be found in Ref. [64].

Prior to calculations, it was important to ensure a consistent definition of the strain recovery length between the DVC measurements and the analytical predictions. In the DVC measurements, the strain recovery lengths on each side of the break was defined as the distances from the break at which the strains recovered 90% of the applied normal strains (i.e. a strain value reduced by 10% relative to the applied normal strain), following Rosen's definition [65] and Schöberl's approach [47]. Accordingly, the distance (z) from the break to the point corresponding to 90% stress recovery (Z_{90}) was determined from the modified Cox's model.

As a first step, the slip length was calculated using equation (3), where D is the fibre diameter, E_f the tensile modulus of the fibre, ε the applied strain in the fibre direction (1.25% based on DVC strain measurements), w the inter-fibre distance (*i.e.* fibre spacing) in a hexagonal fibre array of cylindrical fibres, and G_m the shear modulus of the matrix (1073 MPa was used from Ref. [21]). The w can be related to the local fibre volume fraction (f) using equation (4).

$$L_s = \frac{D}{4}\left(\frac{E_f \varepsilon}{\tau_0} - 2\sqrt{\frac{E_f w}{G_m D}}\right) \tag{3}$$

$$w = D\left(\frac{1}{\sqrt{f}}\sqrt{\frac{\pi}{2\sqrt{3}}} - 1\right) \tag{4}$$

To determine the local fibre volume fraction, Voronoi tessellation [66,67] was performed in ImageJ (*Voronoi* algorithm) on eight single fibre breaks analysed in each of the low and high interfacial strength materials, yielding f values ranging from 50% to 70%. Accordingly, w/D ratios corresponding to f values of 50%, 55%, 60%, 65%, and 70% were used for parametric analysis of recovery length (Z_{90}). Given that the exact shear-sliding resistance near the break in the actual bulk composites was uncertain, τ_0 was varied from 50 MPa to 200 MPa to assess the sensitivity of the recovery length (Z_{90}). The interfacial shear strength measured from the SFFTs (see Table 3), together with the value of 81.2 ± 5.8 MPa reported in Ref. [68] for another type of carbon fibre/epoxy

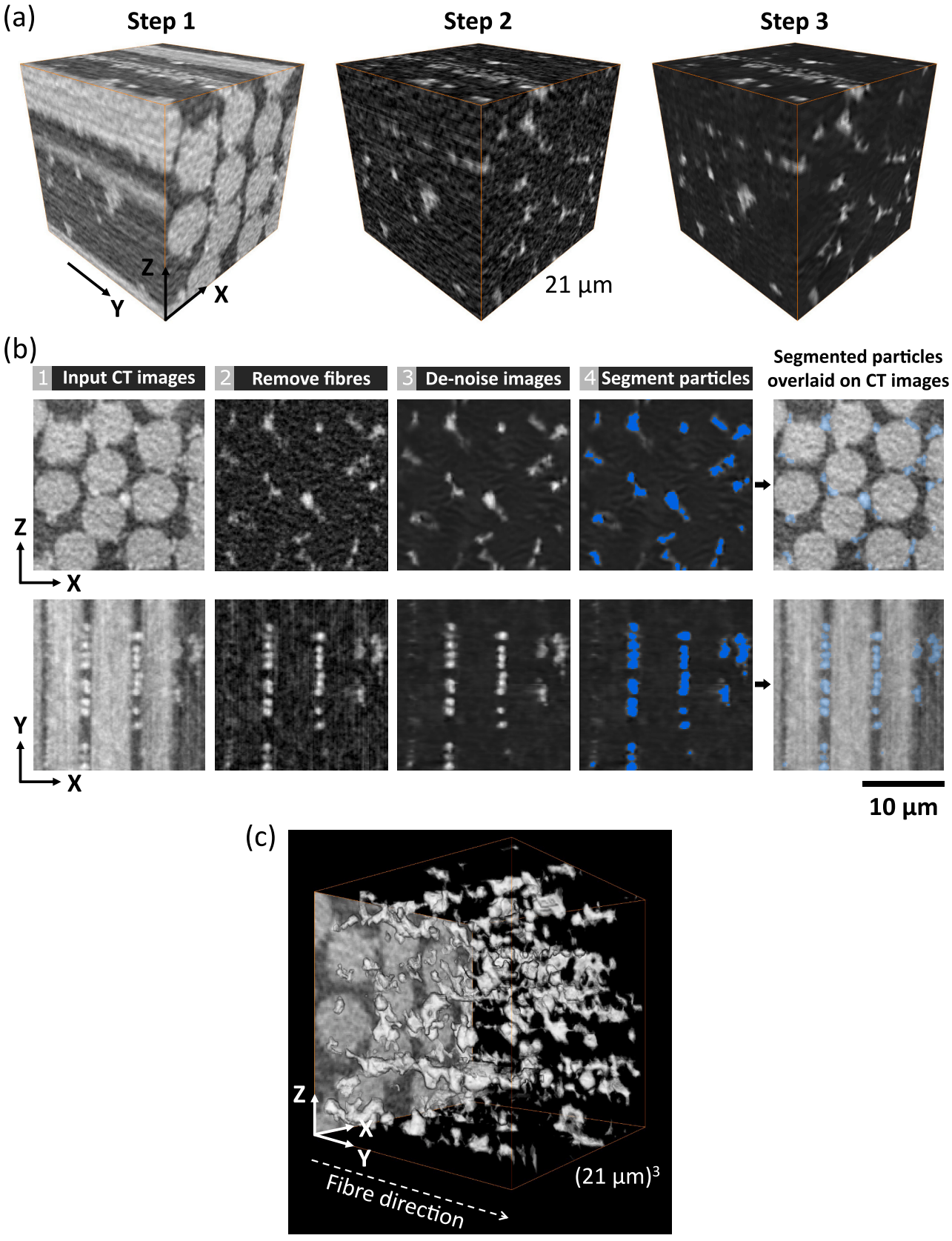

Fig. 4. (a) SRCT NFP cubic volumes (150 nm voxel size) of SiO_2-doped material with low interfacial strength, corresponding to the DVC sub-volume size (21 µm), shown at processing steps 1-3 outlined in (b). **(b)** Schematic illustrating the SiO_2 particle segmentation process used to visualise distribution, performed in Avizo using the SRCT NFP volumes, and **(c)** 3D visualisation of segmented SiO_2 particle features and clusters within a cubic volume matching the DVC sub-volume size (21 µm).

(T700S/Araldite-F) composites, was considered when selecting the range of τ_0 values. Using the obtained slip length, equation (5) was used to derive the expression for the recovery length (Z_{90}), where the fibre stress σ_f was substituted by 0.9 $E_f\varepsilon$. The derived expression is presented in equation (6).

$$\sigma_f = \begin{cases} 4\tau_0\dfrac{z}{D}, & 0 \le z \le L_s \\ E_f\varepsilon - 2\tau_0\sqrt{\dfrac{E_f w}{G_m D}}\,exp\left[2\sqrt{\dfrac{G_m D}{E_f w}}\left(\dfrac{L_s}{D}-\dfrac{z}{D}\right)\right], & L_s \le z < \infty \end{cases} \quad (5)$$

$$\frac{Z_{90}}{D} = \frac{L_s}{D} - \frac{1}{2}\sqrt{\frac{E_f w}{G_m D}}\,ln\left[\frac{0.1E_f\varepsilon}{2\tau_0\sqrt{E_f w/G_m D}}\right] \quad (6)$$

3. Digital volume correlation

3.1. DVC input preparation and processing workflow

DVC requires at least two input volumes for correlation, namely an undeformed (reference) and a deformed volume. Prior to preparing DVC input volumes, seven reconstructed volumes acquired before unloading (steps 1-3) and after unloading (steps 1′- 4′) were registered in Avizo software using *Register Images* module with a 3D rigid transform, configured with "Correlation" and "Quasi-Newton" as the metric and optimiser ports, respectively. This volume registration process ensures that DVC (i.e. displacement tracking) is carried out within the same spatial region. Given that the displacement of particles near fibre breaks is of primary interest, DVC volume preparation began by identifying break sites in the reconstructed volume at the loaded state. A volume of interest (VOI) measuring 500 × 500 × 500 voxels was then selected, and the corresponding VOIs were accordingly cropped from the reconstructed volume across all seven load steps using ImageJ software.

DVC was performed on the prepared input volumes using the commercial software DaVis v10.2.0 (LaVision Ltd., Göttingen, Germany). As a preliminary step, the software divides the input volumes into smaller cubic sub-volumes, forming the basis for matching speckle patterns. The correlation algorithm employs a multi-step, multi-pass strategy to identify matched sub-volumes between undeformed and deformed volumes. In this approach, a Fast Fourier Transform (FFT) is first applied for a global pre-shift, followed by Direct Correlation (DC) for successive refinement. The FFT is used to estimate large-scale shifts of speckle patterns in the deformed volume, such as rigid body displacement, by operating on larger sub-volumes. Subsequently, the DC refines the initial estimate of displacement through iterative matching of sub-volumes, using updated parameters (*e.g.* search radius, sub-volume size, number of passes, overlap value, etc) at each iteration. Further details on Lavision's DVC implementation of the FFT and DC algorithms, along with the DVC parameters, are provided in Refs. [69,70].

Table 5 presents the DVC input parameters used for correlation. As described earlier, the correlation algorithm started with dividing the input volumes into smaller cubic sub-volumes, based on the user-defined sub-volume sizes. The correlation was performed using one FFT step followed by three successive DC steps. For DVC processing to estimate strain around fibre breaks, the sub-volume size during the DC steps was incrementally reduced from 48 voxels to 40 voxels, and finally to 32 voxels. Section 4.2 will provide details of the selection of the final sub-volume size of 32 voxels. Concurrently, the search radius was decreased at each correlation step. To achieve higher spatial sampling, the overlap between adjacent sub-volumes was set to 75%. The 'relative-to-first' correlation mode was selected, by which each deformed volume was correlated with the initial undeformed volume (*i.e.* reference). No smoothing-related post-processing methods, such as strain window adjustment or interpolation, were applied during the DVC strain computation.

3.2. DVC uncertainty measurement (noise and sensitivity)

The measurement of DVC strains, based on *in situ* tomographic volumes, requires quantifying uncertainties such as intrinsic noise and bias, which may arise from the imaging system (*e.g.* scattered radiation, electronic noise, fluctuating beam intensity, imperfect optics) or the experimental environment (*e.g.* vibrations from rotating stages, thermal instabilities). Such uncertainties can introduce false strains, obscuring the interpretation of strain fields around fibre breaks. It is therefore essential to assess uncertainty levels to establish the range of reliability in DVC strain measurements. To assess the uncertainties, two zero-strain pair analyses were conducted: stationary tests and rigid body displacement, in line with the procedures described in Ref. [47]. Although both low and high interfacial strength materials were studied in this work, only the former was used for uncertainty measurements, as both materials were expected to provide comparable DVC performance.

3.2.1. Stationary test

As an initial step in the stationary test, the specimen was scanned twice at the same FOV position under preload conditions (*i.e.* step 1 in Fig. 3a), with no changes in CT parameters (see section 2.3). The two repeat scans were subsequently correlated using DaVis software with sub-volume sizes ranging from 12 to 80 voxels. For this correlation, the DVC-measured displacement vector fields and computed strains should ideally be zero. In practice, however, the measured values are never exactly zero due to the noise and bias discussed above. Any deviations from zero can, therefore, be regarded as DVC uncertainties, quantified by calculating the standard deviation of strain components in the fibre longitudinal direction (ε_{yy}).

In DVC, displacements are computed by tracking the movement of speckle patterns within sub-volumes between undeformed and deformed volumes. Given that the correlation is performed over a sub-volume, the resulting DVC displacements represent spatially averaged values of the local displacements within the sub-volume. As such, DVC strains are spatially filtered estimates of the real local strains rather than the true strains [71]. Accordingly, the effects of sub-volume size on strain fields must be considered when selecting the sub-volume size to

Table 5
Summary of FFT and DC settings used in multi-step, multi-pass based DVC.

Sub-volume size [voxels]					Binning [voxels]			Search radius [voxels]			Number of passes		
Final	FFT-shift	Step 1	Step 2	Step 3	Step 1	Step 2	Step 3	Step 1	Step 2	Step 3	Step 1	Step 2	Step 3
12	48	48	24	12									
16	64	48	24	16									
20	64	48	32	20									
24	48	48	32	24									
32	64	48	40	32	4 × 4 × 4	2 × 2 × 2	NONE	8	6	4	1	2	4
44	64	64	56	44									
48	96	80	56	48									
52	80	80	64	52									
80	128	112	96	80									

ensure reliable measurement and interpretation. This relationship reflects a fundamental trade-off between spatial resolution (*i.e.* sub-volume size) and strain precision (*i.e.* strain uncertainties). A larger sub-volume size leads to greater averaging of voxel displacements, which lowers the strain precision and reduces sensitivity to detecting local strains around fibre breaks. Conversely, a smaller sub-volume size results in higher strain uncertainties as fewer speckle patterns are available in these regions. To identify the sub-volume size that best balances these trade-offs, strain uncertainties were evaluated across a selected range of sub-volume sizes, which will be further discussed in section 4.2.

3.2.2. Rigid body displacement

After completing the repeat scans, the tested specimen was mechanically translated by 9 pixels (≈ 5.85 μm) in the loading direction (Y-axis). This translation was achieved by digitally commanding the translation/rotation stage (see Fig. 2a), after which an additional scan was performed with no changes in FOV position and CT parameters. The induced Y-displacement was manually verified by tracking the shift of unique features (*e.g.* a distinctive void or individual SiO_2 particles) between the pre- and post-translation scans, following the approach used by Schöberl et al. [47]. A repeat scan from the stationary test and a translated scan were subsequently correlated using DaVis software with varying sub-volume sizes from 32 to 80 voxels. This was to enable assessment of displacement vector fields and uncertainties associated with DVC processing under known displacement conditions. As in the stationary test, the resulting DVC uncertainties in displacement (U_y) and strain (ε_{yy}) were evaluated across a selected range of sub-volume sizes.

4. Results and discussion

4.1. Particle distribution analysis

Fig. 1b and **c** shows representative slices extracted from the 3D reconstructed volumes acquired at a 650 nm voxel size, illustrating qualitative differences in particle distribution and agglomeration between the SiO_2- and $BaTiO_3$-doped (reference) CFRPs. The SiO_2 loaded microstructures exhibited a visually more uniform distribution with reduced agglomeration, a tendency that was evident within volumes of the same scale as the DVC sub-volume size used in this study (see Fig. 4b). Particle counting across 10 randomly located NFP volumes identified an average of 216 ± 17 particle features within a representative DVC sub-volume of 21 × 21 × 21 μm^3, *i.e.* indicative of the particles being sufficiently finely and consistently dispersed to support correlation at these length-scales. In contrast, the $BaTiO_3$ particles tended to exhibit particle clusters, with Fig. 1c for example evidencing an agglomeration of ~20 μm. As such, the $BaTiO_3$ loaded material showed regions of low fibre volume fraction (fibres being displaced by agglomerations), and regions of sparse particle density. As the occurrence of such regions increases, DVC performance may be expected to deteriorate (*i.e.* in terms of the representativeness and the trackability of different regions). Thorough visual inspection of all SRCT volumes obtained of the SiO_2-containing materials revealed no single agglomeration larger than ~3 μm and in any of the specimens tested, *i.e.* significantly smaller than seen in the $BaTiO_3$ materials. In terms of contrast, $BaTiO_3$ particles did however demonstrate higher greyscale differentiation against the fibres than the SiO_2 particles, which may then be expected to improve speckle pattern tracking/correlation based on greyscale values.

Although segmented SiO_2 particles from the 150 nm NFP volumes (see section 2.4) were available, a formal quantitative assessment of their distribution and agglomeration was not carried out in this study as this would require comparable data characterising the distribution of alternative fiducial particles such as $BaTiO_3$. Obtaining such data would require CT datasets acquired at a voxel size sufficient for reliable particle segmentation, which were not available at the time of writing. Ten randomly located NFP volumes are publicly available in a Zenodo dataset [72] for further independent analysis.

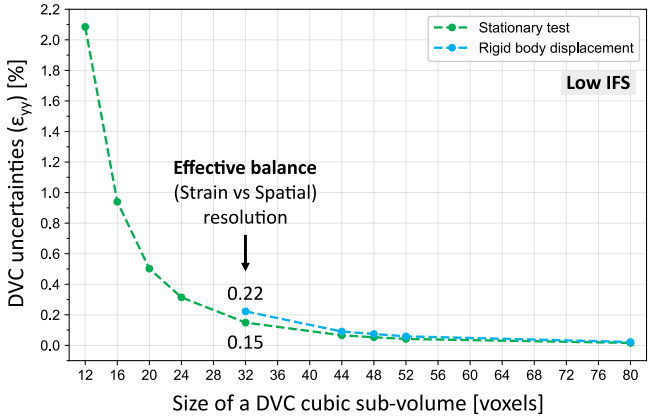

Fig. 5. Variations of DVC uncertainties with cubic DVC sub-volume sizes, measured using low interfacial strength (IFS) material, under stationary and rigid body displacement tests. The 'effective balance' denotes the point assumed to provide a practical trade-off between strain and spatial resolution in DVC.

4.2. DVC uncertainty assessment

4.2.1. Stationary tests

Fig. 5 shows the variation in DVC strain uncertainties as a function of cubic sub-volume size in the range of 12 to 80 voxels, where uncertainty is based on the standard deviation of apparent strain values. The normal strain 'ε_{yy}', parallel to the fibre load direction, is of particular interest, as load redistribution around fibre breaks occurs predominantly in this direction. Uncertainty exhibits a decreasing trend as the sub-volume size increases, reflecting the trade-offs between strain precision and spatial resolution previously discussed in Section 3.2.1. For this work, a nominal uncertainty threshold/target was identified as ~0.2%, corresponding to ~10% of the typical macroscopic ~2% failure strain of a carbon fibre composite. Accordingly, a sub-volume size of 32 voxels (corresponding to 20.8 μm) was selected, yielding strain uncertainties of ~0.15%, which was deemed to provide an effective balance between strain and spatial resolution. The maximum applied macroscopic strain at the final *in situ* scan load, as measured via DVC, was ~1.4%.

As a preliminary step to assess the DVC applicability of SiO_2 particles, the measured uncertainty levels were compared with CFRPs doped with 7.5 wt% $BaTiO_3$ particles, as reported by Schöberl et al. [47]. It is noted that Schöberl et al. used the same DaVis correlation algorithm and a voxel resolution of 650 nm. As expected, the strain uncertainties of SiO_2-doped CFRPs exhibit a similar decreasing trend with increasing sub-volume sizes, consistent with those reported for $BaTiO_3$-doped CFRPs. At the same sub-volume size of 32 voxels, the present study, which introduces SiO_2 particles, yielded higher uncertainty level of ~0.15% than the 0.085% reported for $BaTiO_3$-doped CFRPs. This discrepancy may be attributed to several factors, such as variations in CT acquisition conditions for the current and previous tests. However, it is clear that the $BaTiO_3$ particles do, as expected, generate much stronger intrinsic contrast, which can be expected to improve DVC tracking. While measured DVC strains using SiO_2-doped CFRPs indicate a lower precision than $BaTiO_3$-doped CFRPs, the use of SiO_2 particles clearly resulted in more uniformly distributed and undisturbed composite microstructure.

4.2.2. Rigid body displacement tests

Fig. 5 also presents the variation in DVC strain uncertainties as a function of cubic sub-volume sizes from 32 to 80 voxels, obtained by correlating CT volumes acquired before and after a rigid body translation of 9 pixels (≈ 5.85 μm) along the Y-axis. In contrast to stationary

tests, sub-volume sizes below 32 voxels were excluded from this analysis, as such small sub-volumes were previously found to yield strain uncertainties substantially exceeding the 0.2% uncertainty threshold. As for the stationary tests, displacement 'U_y' and normal strain 'ε_{yy}' in the Y-direction were analysed.

At a sub-volume size of 32 voxels, DVC measured an average U_y displacement of 8.46 pixels (≈ 5.5 μm) with standard deviation of 0.002 pixels (≈ 0.001 μm), remaining nearly identical across all studied sub-volume sizes. This DVC-estimated displacement agrees well with the range of 9 ± 1 pixels (≈ 5.85 μm ± 0.65 μm) determined through manual tracking of features in the CT data. In terms of strain uncertainties, a sub-volume size of 32 voxels resulted in an uncertainty level of 0.22%, *i.e.* slightly higher than the 0.15% measured in the stationary test. This trend of slightly elevated uncertainties under rigid body displacement, relative to the stationary test, is also consistent with previous studies [47,69,73,74], which attributed similar increases in uncertainty to the additional interpolation errors introduced by the correlation algorithm in the presence of specimen movement.

4.3. DVC strain assessment around single fibre breaks

4.3.1. DVC methodological framework for strain recovery length analysis

As described in section 3.2.1, the DVC algorithm spatially averages local displacements within sub-volumes. This implies that strain measurement accuracy near fibre break sites can be influenced not only by the surrounding speckle patterns but also by the fibre break features and the severe strain gradients expected to arise around individual fractured fibres. In this respect, it is important to delineate the scope of the current DVC strain measurements. With DVC sub-volume sizes on the order of 21 μm (see section 4.2) and a fibre diameter of ~5.4 μm, it can be seen that the sub-volumes are inevitably limited in their ability to represent the displacements/strains within the most severely deformed regions adjacent to a single fibre break. As such, even small relative shifts in the sub-volume location (defined by a pixel-based grid) and in the break site (stochastically occurring within the imaged region) will inevitably lead to substantial variations in the magnitude of apparent strains close to fibre breaks. Therefore, the objective here is not to report apparent strains 'ε_{yy}' in the immediate vicinity of the actual break site, but rather to assess the region *remote* from the break, to determine the distance at which the strain disturbance returns to the background level (i.e. applied material-level strain). In other words, this measurement focuses on interrogating regions where the strain gradient from the break site approaches zero, meaning that the effects of sub-volume size and location become less critical.

DVC analysis by Schöberl et al. [47] presented a method using an algorithmic mask during correlation to isolate and disregard the open crack/cavity created at a break site. The rationale is that strain cannot, of course, be computed in regions where material is 'absent'. Although previously proposed, masking of fibre breaks was not employed in the present study, as its effect on strain measurements was found to be negligible. As noted above, the primary focus of this study was not on mapping of strain values immediately adjacent to a break, but capturing the strain recovery length, where longitudinal strains return to background levels. Herein, the strain recovery length is conceptually equivalent to the ineffective length [75]. It may be noted that DVC strains in this work were derived from speckle patterns in the matrix rather than from the broken fibre itself. Therefore, in the present work, the ineffective length is referred to as the 'strain recovery length'.

Following the uncertainty measurement in section 4.2, strain fields around single fibre breaks were computed using a sub-volume size of 32 voxels with 75% overlap, i.e., a step size of 8 voxels, corresponding to a 5.2 μm separation between individual displacement measurement point. Fig. 6 illustrates two representative DVC strain maps near a single fibre break, selected from the complete set spanning the entire DVC volume. Each map corresponds to the same load level of 87% UTS, with one acquired prior to unloading (Fig. 6a) and the other after unloading and reloading to that load (Fig. 6b), and both were overlaid with the microstructure of a high interfacial strength material. No smoothing methods, such as adjustment of the virtual strain gauge size, were applied to the measured strains.

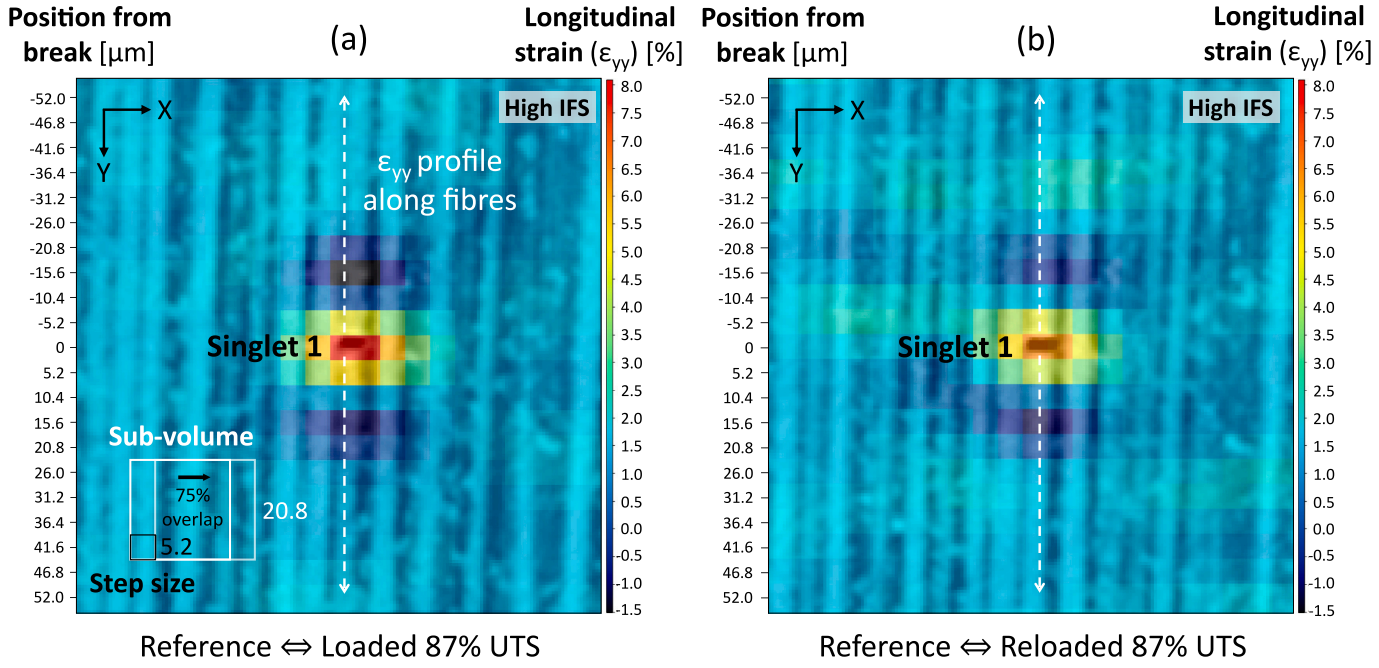

Fig. 6. (a) DVC strain map generated by correlating volumes scanned at steps 1 and 2 (as shown in Fig. 3), illustrating the ε_{yy} longitudinal strain fields surrounding Singlet 1 in high interfacial strength (IFS) material at 87% UTS. The white square indicates a DVC sub-volume sized 20.8 μm, while the black square marks the step size resulting from 75% sub-volume overlap. The white dashed line shows the fibre direction along which a line profile of ε_{yy} strain was extracted. The X-position of the strain profile is defined relative to the break location, which is set as the origin. **(b)** DVC strain map surrounding the same Singlet 1, generated by correlating volumes scanned at step 1′ and 2′ after unloading.

The applied normal strains at each load level were computed using DVC, hereafter referred to as 'far-field strain'. Strain values were extracted as the average of four sets of sub-volumes surrounding the break site but located outside the region affected by strain recovery. Each set consisted of at least five sub-volumes in the width, length, and out-of-plane directions, positioned laterally and vertically on both sides of the fibre break (i.e. ~60 μm transversely and ~90 μm longitudinally away from a given break).

4.3.2. *Strain recovery lengths in low and high interfacial strength materials*

To measure the strain recovery length, a longitudinal line profile of apparent ε_{yy} strains was first extracted from the strain maps along the sub-volumes, referenced to the position of the sub-volume nearest to the fibre break centre coordinate. This procedure was repeated across all load levels for eight isolated single fibre breaks, which were identified within the scan volume of both the low and high interfacial strength materials at the lowest scan load level. Fig. 7 illustrates the resulting strain profiles for the low and high interfacial strength materials at 89% and 87% UTS, respectively, prior to unloading. The strain profiles show a nearly symmetrical pattern about the fibre break plane. Each strain profile as a function of distance from the break plane exhibits a peak at the break location, followed by a decrease and subsequent recovery towards the far-field strain level.

As noted previously in section 4.3.1, the severely localised strain gradients immediately adjacent to the fibre breaks, together with the presence of a physical discontinuity, will inevitably have a marked influence on the *apparent* deviation of strain from the far-field value. This effect is particularly pronounced because the scale of DVC sub-volumes and their 75% overlap generate strain calculation points at distances (5.2 μm) comparable to the fibre diameter, *i.e.* the defining length-scale of crack/discontinuity. Accordingly, the observed strain peaks at the break location in Fig. 7 are interpreted as anomalous rather than reflecting real material deformation.

Following this peak strain, the strain profiles exhibited a consistent trend whereby higher peak strains were accompanied by deeper trough strains, often extending into negative values. These strain distribution trends, particularly the negative strains that are not physically reasonable, may arise from constraints imposed by the correlation algorithm, which enforces compatibility of strains within the discontinuity region through mechanical regularisation [71,76]. The enforced compatibility condition, combined with the overly high strain estimates at the fibre break, leads to the requirement of a negative strain at some point between the peak and the far field. Schöberl et al. [47] similarly reported a strain distribution in the vicinity of the break, characterised by negative

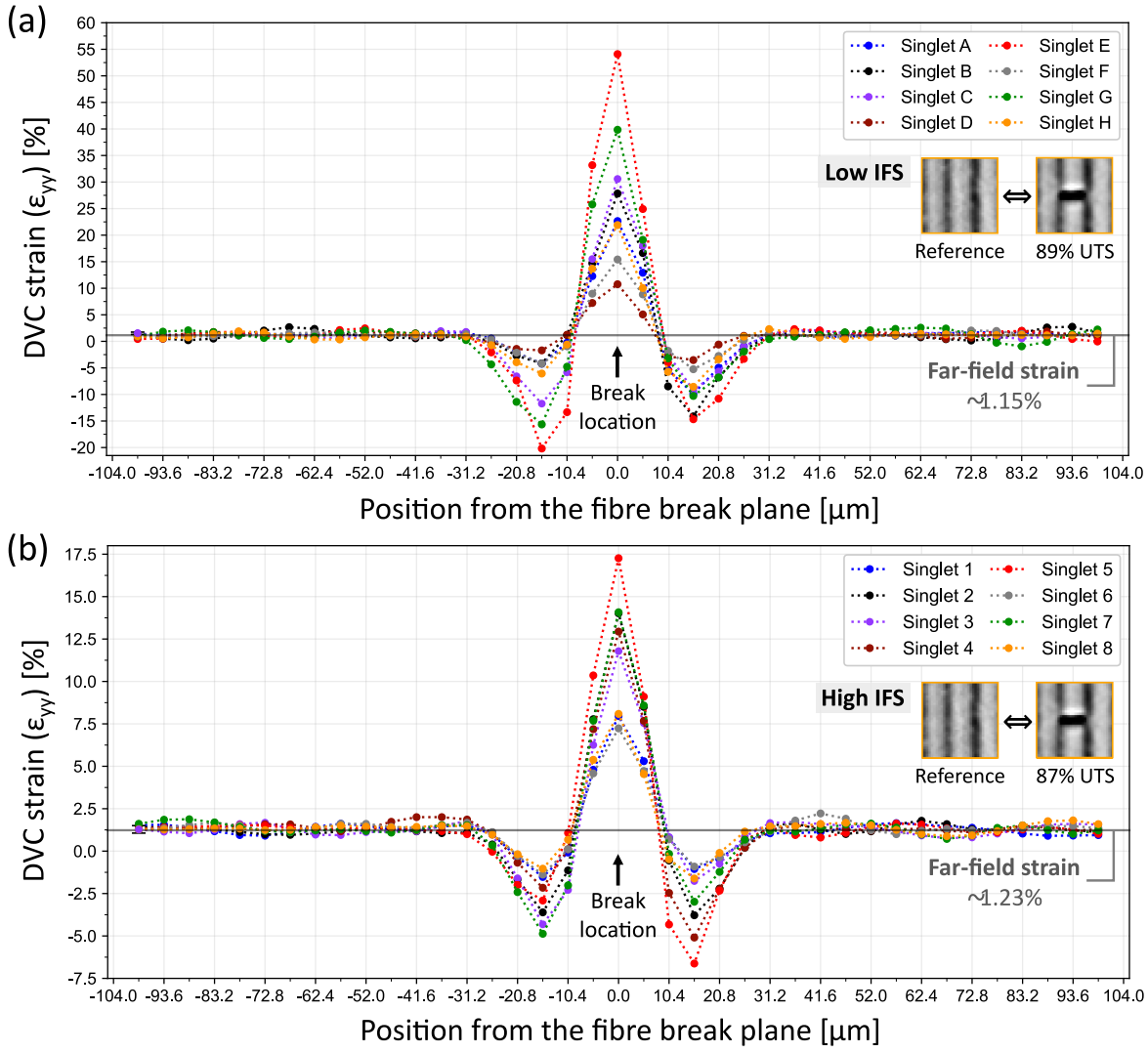

Fig. 7. Line profiles of ε_{yy} strain extracted from (a) Singlets 'A to H' in low interfacial strength (IFS) material at 89% UTS, with far-field strains of ~1.15% and (b) Singlets '1 to 8' in high IFS material at 87% UTS, with far-field strains of ~1.23%. The X-axis follows the same positional definition as in Fig. 6. Both DVC strain fields were obtained by correlating volumes scanned before unloading.

Table 6
Comparative summary of peak strains at fibre break location and corresponding opening distances for singlets (A, E, G) in low and singlets (2, 3, 4) in high interfacial strength (IFS) materials, measured at respective scan load levels.

Scan load	89% UTS		94% UTS	
Low IFS	Peak strain at fibre break [%]	Fibre break opening distance [μm]	Peak strain at fibre break [%]	Fibre break opening distance [μm]
Singlet A	22.7	2.9	24.3	3.3
Singlet E	54.1	3.3	56.2	3.3
Singlet G	39.8	3.9	36.5	3.3
Scan load	**87% UTS**		**92% UTS**	
High IFS	Peak strain at fibre break [%]	Fibre break opening distance [μm]	Peak strain at fibre break [%]	Fibre break opening distance [μm]
Singlet 2	14.0	3.3	17.0	2.6
Singlet 3	11.8	3.3	14.8	3.6
Singlet 4	12.9	2.9	13.9	3.3

trough strains following higher peak strains. It is also notable that this artefact is not observed in the ongoing higher-resolution DVC analysis at 150 nm [77], where particle displacements may be expected to be represented more accurately between DVC sub-volumes due to the higher-resolution speckle patterns. Table 6 presents peak strain levels and corresponding fibre break opening distances for several single fibre breaks among those analysed in Fig. 7. No direct correlation was evident between the extent of discontinuity, represented by the measured fibre break opening distance, and the level of the peak strain values, consistent with artefacts inherent to the DVC algorithm and/or severe strain gradients determining apparent strain values when measured very close to a fibre break.

While the exact magnitudes of strain disturbances around individual breaks were found to be variable, the distance over which strain returned to the far-field value (*i.e.* strain recovery length) was reasonably consistent across all analysed breaks; estimated to be ~31 μm on either side of the break location along the loading direction. Although the strain distributions around fibre breaks appeared nominally symmetric, appreciable deviations were observed in the individual strain profiles, with oscillatory variations in regions remote from the break location. These variations may arise from a combination of factors, including measurement uncertainties and microstructural variations (*e.g.* speckle pattern distribution, fibre misalignment).

To characterise the strain recovery length in greater detail, folding and averaging procedures were applied to the strain profiles to mitigate the influence of these variations on strain recovery measurements. Using the break location identified in Fig. 7 as the reference plane, strain values from sub-volumes located on the upper side of the break plane (*i.e.* at negative positions from the break plane) were combined with those from equidistant sub-volumes located on the lower side of the break plane (*i.e.* at positive positions from the break plane), in what we refer to as the 'folding' step. These combined strains were subsequently averaged (*e.g.* strain values from sub-volumes positioned at −10.4 μm and 10.4 μm) and plotted as a function of distance from the break plane (*i.e.* positive positions from the break plane), in what we refer to as the 'averaging' step. These folding and averaging procedures were consistently applied to strain profiles obtained before and after unloading at all load levels, as shown in Fig. 8.

Fig. 8a and b presents the folded and averaged strain fields for low and high interfacial strength materials at 89% and 87% UTS, respectively, prior to unloading. As explained earlier in section 2.5, the strain recovery length was defined as twice the distance from the break location to the point where the strains recovered 90% of the far-field value. This reflects the region where the responses of the broken fibre and surrounding matrix are estimated to transition from local inelastic to bulk elastic behaviour.

The half strain recovery lengths were measured from the resulting strain fields and were consistently ~31 ± 5.2 μm across both material types, highlighting two key observations. First, the measured lengths are of the same order as the 37 μm reported for $BaTiO_3$-doped CFRPs. Second, for these bulk composite materials, strain recovery lengths for single fibre breaks were insensitive to the range of interfacial strength indicated by single fibre tests (see Table 3).

4.3.3. *Effect of discontinuities on DVC strain fields and strain recovery length*

Fig. 8c and d presents the strain fields at the same singlets analysed above, obtained after unloading and subsequent reloading to 89% and 87% UTS in low and high interfacial strength materials (see Section 2.3). Singlets 'D and F' in low and singlet '6' in high interfacial strength materials were excluded from strain field extraction, as they developed into cluster breaks at 94% and 92% UTS prior to unloading, meaning that their strain profiles could no longer be regarded as representative of isolated singlets. The resulting strain fields exhibited lower peaks and shallower troughs than those obtained from DVC analysis using reference volumes scanned before unloading. This is again consistent with the peak strain at the break location and the accompanying negative trough strain adjacent to it, being artefacts arising from the DVC operating near its resolution limits around the fibre break, together with the dominant influence of the fibre break ends. Despite variations in strain peaks and troughs, both materials however maintained half strain recovery lengths of ~31 μm and showed similar strain profiles within this region, consistent with earlier measurements obtained without discontinuities in the reference volume.

To further highlight the strain recovery trends shown in Fig. 8a–d, we additionally averaged strain profiles pointwise at each distance from the break plane, forming a single representative strain profile. Fig. 8e illustrates the resulting representative strain profiles around the singlets identified within each low and high interfacial strength materials before and after unloading. These findings suggest that although discontinuities significantly magnified apparent strains immediately adjacent to fibre breaks, their effects are negligible when determining strain recovery lengths away from the break.

4.3.4. *Mechanistic interpretation and assessment of DVC-estimated strain recovery lengths*

4.3.4.1. Strain recovery lengths in low and high interfacial strength materials. To examine how strain recovery varies with load, half recovery lengths were measured at two higher load levels for the same singlets, which were previously described at 89% and 87% UTS, in the low (89%, 94%, 99% UTS) and high (87%, 92%, 97% UTS) interfacial strength materials. In the low interfacial strength material, singlets 'D and F' developed into cluster breaks from 94% UTS onward and were therefore

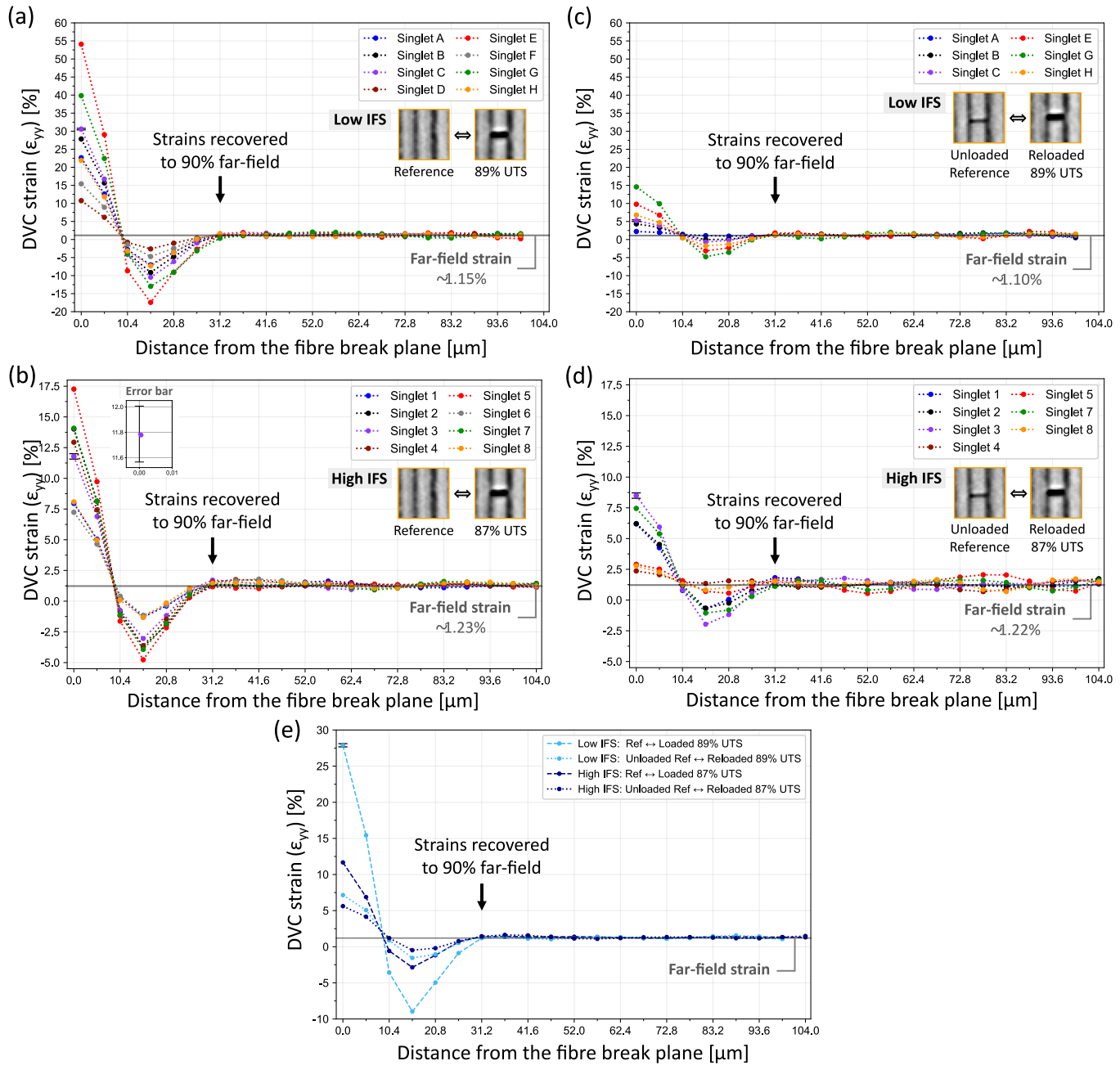

Fig. 8. Line profiles of ε_{yy} strain, obtained by folding and averaging, illustrating strain recovery from the fibre break plane. Strains were extracted from DVC before unloading at **(a)** singlets 'A to H' in low interfacial strength (IFS) material (89% UTS) and **(b)** singlets '1 to 8' in high IFS material (87% UTS). From DVC after unloading, strains were identically extracted from the same singlets in **(c)** low IFS material (89% UTS) and **(d)** high IFS material (87% UTS). Singlets that developed into clusters prior to unloading were excluded in (c) and (d). **(e)** Overview of strain recovery trends at singlets before and after unloading, obtained through additional averaging of the averaged/folded strains identified in (a) to (d).

excluded from strain field extraction. In the high interfacial strength materials, singlet '6' and singlets '1 and 7' formed clusters from 92% to 97% UTS, respectively, and were likewise excluded from strain field extraction. It should be noted that, as outlined in section 2.3, the load history to reach the highest load levels (99% and 97% UTS) included an unloading step (see Fig. 3), but this was found to have no discernible influence on the strain recovery lengths. Following the approach used in Fig. 8e, averaging was applied separately to the extracted strains at singlets in low and high interfacial strength materials at each load level.

Fig. 9 illustrates the averaged strain gradients for the low and high interfacial strength materials across all load levels. Again, the focus here is not on the magnitude of peak strains and strain disturbances adjacent to the break, but rather on comparing the strain recovery lengths. Nevertheless, it is informative to briefly explain the strain redistribution varying with loads. Peak strain levels at the break location increased at 94% and 92% UTS in the low and high interfacial strength materials, respectively, compared with lower load levels. This increase is attributed to the further opening of fibre break ends with increasing load, potentially accompanied by additional damage, which together increased the extent of discontinuities. In contrast, strain gradients at 99% and 97% UTS exhibited markedly reduced peak strain values, attributable to the use of a DVC reference volume that contained residual discontinuities from reclosed break ends after unloading. Even when accounting for the 2% UTS higher scan load level in the low

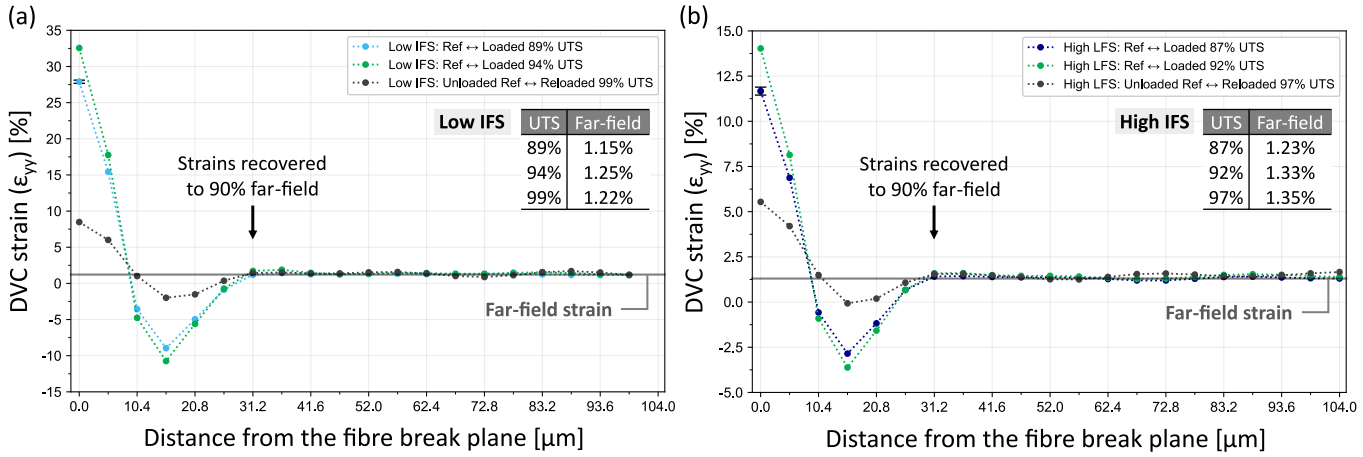

Fig. 9. Line profiles of ε_{yy} strain at singlets in (a) low interfacial strength (IFS) material (89%, 94%, and 99% UTS), and (b) High IFS material (87%, 94%, and 99% UTS), illustrating strain recovery with increasing loads. The strain profiles were obtained through additional averaging of the averaged/folded strain profiles extracted from singlets 'A to H' and '1 to 8' at each load level, following the approach used in Fig. 8e. Far-field strain values across all load levels for low and high IFS materials are presented in inset tables in (a) and (b).

interfacial strength material, its peak strain values remained significantly higher than those measured for the high interfacial strength material at all load levels. However, whether these differences primarily stem from damage associated with weaker adhesion is uncertain. Although peak strain values varied, the half strain recovery lengths consistently remained at ~31 μm in both low and high interfacial strength materials across all higher load levels.

4.3.4.2. Interfacial debond identification and DVC resolution limitations. To examine the effects of interfacial strength on strain recovery lengths using DVC, it is valuable to understand how DVC may detect such differences through interfacial phenomena such as debonding. Debonding constitutes a key mechanism that may be expected to affect longitudinal strain variations within the strain recovery region, and hence the associated DVC measurements. When debonding occurs, there is a physical discontinuity between fibre and matrix, with failure of the chemical bonds and relative sliding and/or opening between fibre and matrix at the interface. Debonding will tend to reduce the high stress in the matrix immediately adjacent to the fibre break and result in a reduced stress gradient over the debonded length, with the potential to produce a smaller stress concentration at the debond tip. Frictional sliding can also play a role, particularly when the displacement at the interface is primarily in shear. Accordingly, the speckle patterns embedded in the matrix adjacent to a bonded interface will exhibit displacements distinct from those for a debonded interface. Although, as previously discussed, the peak DVC strain values near the fibre break are not believed to be accurate, the fact that there is a consistent pronounced peak (of whatever magnitude) suggests that there is little or no debonding in either of the materials around isolated fibre breaks under the applied stresses.

The inference of little or no debonding is consistent with observations from our previous work. Lee et al. [78] recently performed synchrotron holotomography imaging with a finer voxel size of 150 nm on the same material (high interfacial strength) used in this study. No significant debonding was observed in any of the fibre breaks imaged, and in no case did it extend more than 1.5 μm from the fibre break ends. In some cases, it was observed that short matrix microcracks and very short interfacial debonds can form contiguously around the same break when it is located near resin-rich pockets. On the side of the break edge adjacent to the resin-rich pocket, matrix microcracks formed and propagated non-uniformly toward these regions. The matrix microcracks extended only ~1.6 μm before terminating with blunted crack tips, suggesting local matrix inelasticity. Short interfacial debonds formed on the opposite side of the break, where the surrounding matrix

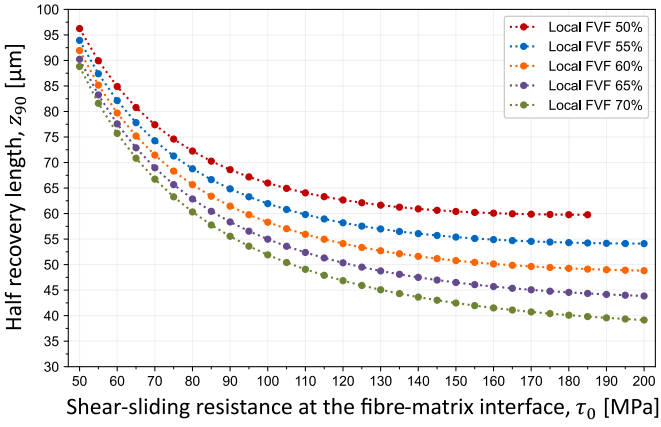

Fig. 10. Analytical half recovery lengths (Z_{90}) on each side of a single fibre break, predicted using the modified Cox shear-lag model, as a function of shear-sliding resistance (τ_0) for five different local fibre volume fractions (FVFs).

was constrained by neighbouring fibres with smaller inter-fibre distances. The debonds extended no further than ~1.5 μm along the fibre, remaining largely confined to the break ends. While it is possible that there was a degree of shear debonding that did not exhibit opening of the fibre-matrix interface (*i.e.* essentially pure shear of the interface), it is considered unlikely given that matrix was precisely adhered to fibre break edges. These higher-resolution observations corroborate the current inference of no detectable large-scale debonds in the low and high interfacial strength materials in the 650 nm scans, while also highlighting the challenges for DVC in discerning such small debonds (~1.5 μm) at 650 nm resolution. Taken together, these findings strengthen the view that limited debond propagation underlies the limited influence of interfacial strengths derived from single fibre tests on strain recovery length measurements.

4.3.4.3. Analytical and numerical corroboration of DVC-estimated strain recovery lengths. Fig. 10 presents the variation of the analytical half recovery length (Z_{90}) as a function of the shear-sliding resistance (τ_0) for five different local fibre volume fractions (FVFs). Overall, the predicted half recovery lengths span from 39 μm to 96 μm across the studied range of shear-sliding resistance and local FVFs. Given the literature-reported τ_0 value of 81.2 ± 5.8 MPa [68], obtained from single-fibre pull-out tests on carbon fibre/epoxy composites, the τ_0 range of 75-85 MPa was first

considered for the comparison. Within this range, the predicted half recovery lengths ranged from 58 μm to 75 μm, which were about 1.5-2.5 times higher than the DVC-estimated recovery length of ~31 μm. However, these discrepancies are primarily attributed to the idealised assumptions of the modified Cox's shear-lag model, including the absence of matrix inelasticity near the break region and the use of hexagonal fibre arrangement. In contrast, the DVC measurements reflect local microstructural heterogeneity, random fibre arrangement, real interfacial conditions in the bulk composite. In particular, Swolfs et al. [15] reported that, in randomly ordered fibres, the nearest intact fibre is located much closer to the broken fibre and accordingly carries higher local stress than in a hexagonal arrangement. This strong local stress redistribution, whereby intact fibres farther from the break are more effectively shielded from overload by the nearest fibre (i.e. shear shielding effect), leads to faster stress recovery in the broken fibre and therefore a shorter recovery length.

It is also worth noting that the effective τ_0 values in the multi-fibre composites (i.e. low and high interfacial strength materials) might have been higher than 75-85 MPa. In multi-fibre composites, the matrix is more strongly confined by the surrounding fibres, which can induce a hardening/stiffening response compared to single-fibre composites. Accordingly, this may elevate the matrix yield stress and, in turn, increase the effective τ_0. While the magnitude of the τ_0 increase remains uncertain, adopting a higher τ_0 results in shorter predicted recovery lengths, bringing them closer to the DVC-estimated values. Overall, although the analytical predictions deviated primarily due to idealised assumptions, the resulting discrepancies were considered reasonable and still support the physical plausibility of the DVC results.

In addition, the DVC-estimated half recovery lengths were compared with fibre break FE models developed by Swolfs et al. [15]. These models incorporated 3D representations of UD randomly packed carbon fibres with a fibre volume fraction of ~55%, and assumed linear elasticity and perfect bonding for matrix and fibres. As such, they provided a more representative stress redistribution response for multi-fibre composites than the modified Cox's shear-lag model. The models predicted that the recovery lengths (i.e. referred to as the ineffective length in Ref. [15]) in a single broken fibre are ~13 and ~9 times the fibre radius (R) at FVFs of 50% and 70%, respectively. Applying these factors to the present material system ($R = 2.7$ μm) gives recovery lengths of ~35 μm and ~24 μm, which are of the same order of magnitude as the DVC-estimated value (~31 μm). Importantly, this apparent consistency between DVC and numerical predictions indicates that, while our previous very high-resolution imaging [78] indicated that non-linear processes occur in very close proximity to isolated break sites (*i.e.* presence of matrix microcracks), linear-elastic assumptions may be sufficient for modelling stress redistribution.

5. Summary and conclusions

This study presents the extended applicability of digital volume correlation using *in situ* synchrotron computed tomography to obtain local strain distributions around fibre breaks in carbon fibre-reinforced polymer composites, by incorporating SiO_2 particles as volumetric speckle patterns. Two CFRP variants, distinguished by fibre surface treatments that altered interfacial shear strength, were examined to assess experimentally how interfacial strength influences load redistribution around fibre breaks.

The applicability of DVC was assessed in three aspects: particle distribution, DVC measurement uncertainty, and strain recovery length around single fibre breaks. First, both the qualitative analyses of SiO_2 particle distribution and its 3D visualisation within a DVC sub-volume demonstrated well-dispersed speckle patterns with minimal agglomeration. Second, SiO_2-doped CFRPs exhibited approximately 1.7 times higher DVC uncertainties than those reported in previous studies using $BaTiO_3$ particles, which is attributable to distinctly reduced image contrast. However, the uncertainties remained within the same order of magnitude, suggesting their capability to provide a technically acceptable level of DVC performance. Third, longitudinal strain profiles mapped around single fibre breaks captured the load redistribution between broken and neighbouring fibres, with strain recovery lengths of the same order of magnitude as those previously observed in $BaTiO_3$-doped CFRPs.

Despite differences in interfacial shear strength, the half strain recovery lengths in low and high interfacial strength materials were consistent across the measured load levels. The observed consistency was attributed to the apparent absence of significant debonds. As supporting evidence, our previous 150 nm holotomography study on the same material revealed at most very limited debond propagation of ~1.5 μm, which in turn explains both the apparent absence of detectable debonds and the apparent insensitivity of DVC-measured strain recovery lengths. While no significant debonding was observed in the present material systems, further investigation of CFRP materials exhibiting more pronounced differences in interfacial shear strength is recommended. Such conditions may promote more distinct debonding behaviour, yet this remains to be verified. If more extensive debonding emerges, the associated strain redistribution may become sufficiently pronounced to be resolved by DVC, thereby offering experimental insight into how interfacial debonding influences load redistribution.

At the present 650 nm voxel size, the spatial resolution and strain precision of DVC around a fibre break is at the current practical limit. To achieve a deeper mechanistic interpretation of the DVC strain fields around fibre breaks, future work could benefit from high-resolution CT-informed micro-mechanics modelling of the fibre breaks region. Such integration represents a further example of a data-rich mechanics approach. To support such future studies, a portion of the SRCT volumes used for the DVC analysis is made publicly available in a Zenodo dataset [79]. Another direction for future work is to employ other synchrotron imaging techniques with advanced phase-contrast retrieval, such as *in situ* holotomography or ptychography, together with finer voxel sizes sufficient to clearly identify fine-scale damage around fibre breaks and at fibre-matrix interface. This could, in turn, further extend the capability of DVC to resolve more reliably the associated local strain fields and load redistribution around fibre breaks. Overall, the present study provides experimental insights into load redistribution under varying interfacial strengths, informing directions for future studies on advancing longitudinal strength models.

CRediT authorship contribution statement

Yeajin Lee: Writing – original draft, Visualization, Methodology, Investigation, Conceptualization. **Yentl Swolfs:** Writing – review & editing, Methodology, Investigation, Conceptualization. **Partha Paul:** Writing – review & editing, Investigation. **Marco Margini:** Writing – review & editing, Resources, Investigation. **Fernando Alvarez-Borges:** Writing – review & editing, Investigation. **Pierre Thibault:** Writing – review & editing, Resources, Investigation. **Yasuhiro Fukuhara:** Writing – review & editing, Conceptualization. **Tsuneo Takano:** Writing – review & editing, Conceptualization. **Naoki Sugiura:** Writing – review & editing, Conceptualization. **Mark N. Mavrogordato:** Writing – review & editing, Supervision, Methodology, Investigation, Funding acquisition, Conceptualization. **Ian Sinclair:** Writing – review & editing, Supervision, Methodology, Funding acquisition, Conceptualization. **S. Mark Spearing:** Writing – review & editing, Supervision, Methodology, Funding acquisition, Conceptualization.

Declaration of competing interest

The authors declare that they have no known competing financial interests or personal relationships that could have appeared to influence the work reported in this paper.

Acknowledgement

The authors would like to acknowledge the contributions from the Mitsubishi Chemical Corporation (Advanced Molding and Composites Laboratory, Aichi R&D centre, Japan) and the dedicated MCC scientists – Yasuhiro Fukuhara, Tsuneo Takano, Naoki Sugiura – for conducting single fibre tensile and fragmentation tests, and for providing sponsorship, material supplies, and technical support. We gratefully acknowledge Erich Schöberl for generously providing the SRCT dataset used in this study. The work leading to this publication was supported by the Engineering and Physical Sciences Research Council (EPSRC, EP/W003333/1). This work is part of a project that has received funding from the European Research Council (ERC) under the European Union's Horizon 2020 research and innovation program (Grant agreement No. 866026). The authors would also like to acknowledge the Henry Royce Institute, established through EPSRC grants (EP/R00661X/1, EP/P025498/1, and EP/P025021/1).

The authors acknowledge the European Synchrotron Radiation Facility (ESRF) for the provision of synchrotron radiation facilities at the ID19 beamline under proposal number MA5711 and ID16A beamline. We greatly appreciate the technical support and insightful advice provided by the beamline scientists at ID19 (Ludovic Broche) and ID16A (Dmitry Karpov) throughout the preparation and execution of the experiments. We also extend deepest gratitude to our colleagues in the MA5711 experiment (Orestis Katsamenis, Marco Endrizzi, Lorenzo Massimi, Fabio De Marco, Vittorio Di Trapani) for invaluable assistance and insightful advice in performing *in situ* SRCT experiments.

The μ-VIS X-Ray Imaging Centre at the University of Southampton is acknowledged for the 3D image acquisition and post-processing tools. Credit is further extended to Erich Schöberl for valuable technical support and invaluable advice during the early stages of this study, particularly in the preparation of synchrotron experiments and DVC analysis. The authors gratefully acknowledge the technicians at the Engineering Design and Manufacturing Centre (EDMC) at the University of Southampton (Simon Beever, Steven Jenkinson, and Amelia Ellis) for their technical support in preparing the specimens through water-jet cutting.

Data availability

The authors have made the SRCT data used for the particle distribution analysis publicly available on Zenodo, and this is clearly stated in the manuscript (Link: https://zenodo.org/records/17566868). The SRCT data used for Digital Volume Correlation are also made publicly available on Zenodo, and this is clearly stated in the manuscript (Link: https://zenodo.org/records/18959885).

References

[1] Mishnaevsky Jr L, Brøndsted P. Micromechanical modeling of damage and fracture of unidirectional fiber reinforced composites: a review. Comput Mater Sci 2009;44(4):1351–9.
[2] Swolfs Y, Verpoest I, Gorbatikh L. A review of input data and modelling assumptions in longitudinal strength models for unidirectional fibre-reinforced composites. Compos Struct 2016;150:153–72.
[3] Weibull W. A statistical distribution function of wide applicability. J Appl Mech. 1951;18(3):293–7.
[4] Curtin WA. Tensile strength of fiber-reinforced composites: III. Beyond the traditional Weibull model for fiber strengths. J Compos Mater 2000;34(15):1301–32.
[5] Watanabe J, Tanaka F, Okuda H, Okabe T. Tensile strength distribution of carbon fibers at short gauge lengths. Adv Compos Mater 2014;23(5-6):535–50.
[6] Scott AE, Sinclair I, Spearing SM, Thionnet A, Bunsell AR. Damage accumulation in a carbon/epoxy composite: Comparison between a multiscale model and computed tomography experimental results. Compos Part a-Appl S 2012;43(9):1514–22.
[7] Fukuda H. Stress concentration factors in unidirectional composites with random fiber spacing. Compos Sci Technol 1985;22(2):153–63.
[8] Lomov SV, Breite C, Melnikov A, Mesquita F, Swolfs Y, Abaimov SG. Clusters and avalanches of fibre breaks in a model of an impregnated unidirectional fibre bundle under tension. Int J Solid Struct 2021;225.
[9] Cox HL. The elasticity and strength of paper and other fibrous materials. Br J Appl Phys 1952;3(3):72.
[10] Hedgepeth JM. Stress concentrations in filamentary structures, national aeronautics and space administration. 1961.
[11] Hedgepeth JM, Van Dyke P. Local stress concentrations in imperfect filamentary composite materials. J Compos Mater 1967;1(3):294–309.
[12] Okabe T, Takeda N, Kamoshida Y, Shimizu M, Curtin WA. A 3D shear-lag model considering micro-damage and statistical strength prediction of unidirectional fiber-reinforced composites. Compos Sci Technol 2001;61(12):1773–87.
[13] Xia Z, Okabe T, Curtin W. Shear-lag versus finite element models for stress transfer in fiber-reinforced composites. Compos Sci Technol 2002;62(9):1141–9.
[14] Swolfs Y, Morton H, Scott AE, Gorbatikh L, Reed PAS, Sinclair I, Spearing SM, Verpoest I. Synchrotron radiation computed tomography for experimental validation of a tensile strength model for unidirectional fibre-reinforced composites. Compos Part a-Appl S 2015;77:106–13.
[15] Swolfs Y, Gorbatikh L, Romanov V, Orlova S, Lomov SV, Verpoest I. Stress concentrations in an impregnated fibre bundle with random fibre packing. Compos Sci Technol 2013;74:113–20.
[16] Breite C, Melnikov A, Turon A, de Morais AB, Le Bourlot C, Maire E, Schöberl E, Otero F, Mesquita F, Sinclair I. Detailed experimental validation and benchmarking of six models for longitudinal tensile failure of unidirectional composites. Compos Struct 2022;279:114828.
[17] Pimenta S. Fibre failure modelling. Numerical modelling of failure in advanced composite materials 2015:193–224. Elsevier.
[18] AhmadvashAghbash S, Breite C, Mehdikhani M, Swolfs Y. Longitudinal debonding in unidirectional fibre-reinforced composites: numerical analysis of the effect of interfacial properties. Compos Sci Technol 2022;218.
[19] Thionnet A, Chou H, Bunsell A. Fibre break processes in unidirectional composites. Compos Appl Sci Manuf 2014;65:148–60.
[20] Nedele MR, Wisnom MR. Three-dimensional finite element analysis of the stress concentration at a single fibre break. Compos Sci Technol 1994;51(4):517–24.
[21] AhmadvashAghbash S, Fazlali B, Mehdikhani M, Swolfs Y. Finite element analysis of the effect of longitudinal debonding on stress redistributions around fibre breaks in randomly packed fibres. Compos Sci Technol 2022;227.
[22] Huang YL, Young RJ. Analysis of the fragmentation test for carbon-fiber epoxy model composites by means of raman-spectroscopy. Compos Sci Technol 1994;52(4):505–17.
[23] VanDenHeuvel PWJ, Peijs T, Young RJ. Analysis of stress concentrations in multi-fibre microcomposites by means of Raman spectroscopy. J Mater Sci Lett 1996;15(21):1908–11.
[24] van den Heuvel PWJ, Peijs T, Young RJ. Failure phenomena in two-dimensional multi-fibre microcomposites. Part 4: a Raman spectroscopic study on the influence of the matrix yield stress on stress concentrations. Compos Part a-Appl S 2000;31(2):165–71.
[25] Mehdikhani M, Aravand M, Sabuncuoglu B, Callens MG, Lomov SV, Gorbatikh L. Full-field strain measurements at the micro-scale in fiber-reinforced composites using digital image correlation. Compos Struct 2016;140:192–201.
[26] Klavzer N, Gayot SF, Coulombier M, Nysten B, Pardoen T. Nanoscale digital image correlation at elementary fibre/matrix level in polymer-based composites. Compos Part a-Appl S 2023;168.
[27] Withers PJ, Bouman C, Carmignato S, Cnudde V, Grimaldi D, Hagen CK, Maire E, Manley M, Du Plessis A, Stock SR. X-ray computed tomography. Nat Rev Methods Primers 2021;1(1):18.
[28] Rosini S, Mavrogordato MN, Egorova O, Matthews ES, Jackson SE, Spearing SM, Sinclair I. In situ statistical measurement of local morphology in carbon-epoxy composites using synchrotron X-ray computed tomography. Compos Appl Sci Manuf 2019;125:105543.
[29] Garcea SC, Sinclair I, Spearing SM, Withers PJ. Mapping fibre failure in carbon fibre reinforced polymers by fast synchrotron X-ray computed tomography. Compos Sci Technol 2017;149:81–9.
[30] Chatziathanasiou T, Lee Y, Villanova J, Stamati O, Ahmadvashaghbash S, Fazlali B, Breite C, Sinclair I, Mavrogordato MN, Spearing SM, Mehdikhani M, Swolfs Y. Questioning the representativeness of damage mechanisms in single-fiber composites via in situ synchrotron X-Ray holo-tomography. Small 2024;20(52).
[31] Chatziathanasiou T, Breite C, Diehl M, Mehdikhani M, Swolfs Y. In situ transverse single-fibre and bundle tests in synchrotron nano-tomography to unravel interfacial debonding in carbon and glass fibre-epoxy composites. Compos Appl Sci Manuf 2025:109024.
[32] Scott A, Mavrogordato M, Wright P, Sinclair I, Spearing S. In situ fibre fracture measurement in carbon–epoxy laminates using high resolution computed tomography. Compos Sci Technol 2011;71(12):1471–7.
[33] Curtin WA. Theory of mechanical properties of ceramic-matrix composites. J Am Ceram Soc 1991;74(11):2837–45.
[34] Buljac A, Jailin C, Mendoza A, Neggers J, Taillandier-Thomas T, Bouterf A, Smaniotto B, Hild F, Roux S. Digital volume correlation: review of progress and challenges. Exp Mech 2018;58(5):661–708.
[35] Xu F. Quantitative characterization of deformation and damage process by digital volume correlation: a review. Theoretical and Applied Mechanics Letters 2018;8(2):83–96.
[36] Madi K, Tozzi G, Zhang QH, Tong J, Cossey A, Au A, Hollis D, Hild F. Computation of full-field displacements in a scaffold implant using digital volume correlation and finite element analysis. Med Eng Phys 2013;35(9):1298–312.
[37] Bay BK, Smith TS, Fyhrie DP, Saad M. Digital volume correlation: three-dimensional strain mapping using X-ray tomography. Exp Mech 1999;39(3):217–26.

[38] Mehdikhani M, Breite C, Swolfs Y, Soete J, Wevers M, Lomov SV, Gorbatikh L. Digital volume correlation for meso/micro in-situ damage analysis in carbon fiber reinforced composites. Compos Sci Technol 2021;213:108944.
[39] Holmes J, Sommacal S, Stachurski Z, Das R, Compston P. Digital image and volume correlation with X-ray micro-computed tomography for deformation and damage characterisation of woven fibre-reinforced composites. Compos Struct 2022;279:114775.
[40] Agyei RF, Hanhan I, Sangid MD. Detecting damage initiation in short fiber composites via in-situ X-ray tomography and digital volume correlation. Compos Commun 2020;22:100524.
[41] Wang P, Wen J, Lei H, Xu B, Liu Y, Yang L, Fang D. Morphology characterization and in-situ three-dimensional strain field monitor of short carbon fiber-reinforced polymer composites under tension. Compos Struct 2021;262:113634.
[42] Wan Y, Madi SE, Madi K, Soete J, Takahashi J, Lomov S, Swolfs Y. Spatial strain distribution and in-situ damage analysis of sheet moulding compounds based on digital volume correlation, vol. 295. Compos Part B-Eng; 2025.
[43] Lee S, Jo E, Ji W. Digital volume correlation technique for characterizing subsurface deformation behavior of a laminated composite. Compos B Eng 2020;194:108052.
[44] Sanchez JFR, Waas AM, Ji W, Hong C, Park M. Synchrotron microtomography results for notched composites under quasi-static and fatigue loading. Compos Struct 2025:119708.
[45] Brault R, Germaneau A, Dupré J-C, Doumalin P, Mistou S, Fazzini M. In-situ analysis of laminated composite materials by X-ray micro-computed tomography and digital volume correlation. Exp Mech 2013;53(7):1143–51.
[46] Schöberl E, Breite C, Rosini S, Swolfs Y, Mavrogordato MN, Sinclair I, Spearing SM. A novel particle-filled carbon-fibre reinforced polymer model composite tailored for the application of digital volume correlation and computed tomography. J Compos Mater 2021;55(14):1907–34.
[47] Schöberl E, Breite C, Melnikov A, Swolfs Y, Mavrogordato MN, Sinclair I, Spearing SM. Fibre-direction strain measurement in a composite ply under quasi-static tensile loading using digital volume correlation and synchrotron radiation computed tomography. Compos Part a-Appl S 2020;137.
[48] Schöberl E, Mavrogordato M, Sinclair I, Spearing S. Fibre direction strain measurement in a composite ply under pure bending using digital volume correlation and Micro-focus computed tomography. J Compos Mater 2020;54(14):1889–912.
[49] Chatziathanasiou T, Demir O, Soete J, Breite C, Mehdikhani M, Diehl M, Swolfs Y. Material representativeness of a polymer matrix doped with nanoparticles as the random speckle pattern for digital volume correlation of fibre-reinforced composites. Compos B Eng 2024;276:111381.
[50] Srisuriyachot J, Chatziathanasiou T, McNair SA, Santana PR, Bénézech J, Swolfs Y, Dolbnya IP, Butler R, Lunt AJ. Synchrotron X-ray diffraction and digital volume correlation of carbon fibre-reinforced polymers for enhanced characterisation of deformation behaviour. Compos B Eng 2025:112703.
[51] Madi SE, Chatziathanasiou T, Vanhulst J, Bravais G, Fayard B, Wevers M, Swolfs Y, Soete J. In situ biaxial tensile testing of composites: coupling X-ray computed tomography and digital volume correlation with finite element simulations. Compos Part B-Eng 2025;306.
[52] Kim P, Doss NM, Tillotson JP, Hotchkiss PJ, Pan M-J, Marder SR, Li J, Calame JP, Perry JW. High energy density nanocomposites based on surface-modified BaTiO3 and a ferroelectric polymer. ACS Nano 2009;3(9):2581–92.
[53] Anjum N, Ajit Prasad S, Suresha B. Role of silicon dioxide filler on mechanical and dry sliding wear behaviour of glass-epoxy composites. Advances in tribology 2013;2013(1):324952.
[54] Kim K-M, Kim HM, Lee W-J, Lee C-W, Kim T-i, Lee J-K, Jeong J, Paek S-M, Oh J-M. Surface treatment of silica nanoparticles for stable and charge-controlled colloidal silica. Int J Nanomed 2014;9(sup2):29–40.
[55] Wright P, Moffat A, Sinclair I, Spearing SM. High resolution tomographic imaging and modelling of notch tip damage in a laminated composite. Compos Sci Technol 2010;70(10):1444–52.
[56] 3M™. Data Sheets- 3M scotch-weld™ structural epoxy adhesive EC-9323 B/A. 2021.
[57] Paleo P MA, Nemoz C, Vigan'o NR, Gitlab ESRF. NABU: ESRF tomography processing software. https://gitlab.esrf.fr/tomotools/nabu/.
[58] Paganin D, Mayo SC, Gureyev TE, Miller PR, Wilkins SW. Simultaneous phase and amplitude extraction from a single defocused image of a homogeneous object. J Microsc 2002;206(1):33–40.
[59] Schneider CA, Rasband WS, Eliceiri KW. NIH image to ImageJ: 25 years of image analysis. Nat Methods 2012;9(7):671–5.
[60] Schindelin J, Arganda-Carreras I, Frise E, Kaynig V, Longair M, Pietzsch T, Preibisch S, Rueden C, Saalfeld S, Schmid B. Fiji: an open-source platform for biological-image analysis. Nat Methods 2012;9(7):676–82.
[61] Stockmar M, Cloetens P, Zanette I, Enders B, Dierolf M, Pfeiffer F, Thibault P. Near-field ptychography: phase retrieval for inline holography using a structured illumination. Sci Rep 2013;3(1):1927.
[62] Stockmar M, Zanette I, Dierolf M, Enders B, Clare R, Pfeiffer F, Cloetens P, Bonnin A, Thibault P. X-ray near-field ptychography for optically thick specimens. Phys Rev Appl 2015;3(1):014005.
[63] Margini M, Karpov D, Swolfs Y, Breite C, Lee Y, Mavrogordato MN, Sinclair I, Spearing SM, Cloetens P, Thibault P. Hard X-ray nanoscale imaging of carbon fibre composites using near-field ptychography. e-Journal of Nondestructive Testing 2024;29(3).
[64] Landis CM, McMeeking RM. A shear-lag model for a broken fiber embedded in a composite with a ductile matrix. Compos Sci Technol 1999;59(3):447–57.
[65] Rosen BW. Tensile failure of fibrous composites. AIAA J 1964;2(11):1985–91.
[66] Mesquita F. Unidirectional interply fibre-hybrid composites: longitudinal tensile failure and interactions between fibre types. Leuven, Belgium: KU Leuven; 2020.
[67] Breite C. Aligning fibre break models for composites with the observable micro-scale material behaviour. 2021.
[68] Deng S, Ye L, Mai Y-W, Liu H-Y. Evaluation of fibre tensile strength and fibre/matrix adhesion using single fibre fragmentation tests. Compos Appl Sci Manuf 1998;29(4):423–34.
[69] Gillard F, Boardman R, Mavrogordato M, Hollis D, Sinclair I, Pierron F, Browne M. The application of digital volume correlation (DVC) to study the microstructural behaviour of trabecular bone during compression. J Mech Behav Biomed 2014;29:480–99.
[70] Fernández MP, Barber AH, Blunn GW, Tozzi G. Optimization of digital volume correlation computation in SR-microCT images of trabecular bone and bone-biomaterial systems. J Microsc 2018;272(3):213–28.
[71] Leclerc H, Périé J-N, Hild F, Roux S. Digital volume correlation: what are the limits to the spatialresolution? Mechanics & Industry 2012;13(6):361–71.
[72] CT dataset for 3D visualisation of particle distributions in carbon fibre-reinforced polymer composites using near-field ptychography. Zenodo; 2025. https://zenodo.org/records/17566868.
[73] Borstnar G, Gillard F, Mavrogordato M, Sinclair I, Spearing S. Three-dimensional deformation mapping of mode I interlaminar crack extension in particle-toughened interlayers. Acta Mater 2016;103:63–70.
[74] Pierron F, McDonald SA, Hollis D, Fu J, Withers PJ, Alderson A. Comparison of the mechanical behaviour of standard and auxetic foams by X-ray computed tomography and digital volume correlation. Strain 2013;49(6):467–82.
[75] Swolfs Y, McMeeking RM, Verpoest I, Gorbatikh L. Matrix cracks around fibre breaks and their effect on stress redistribution and failure development in unidirectional composites. Compos Sci Technol 2015;108:16–22.
[76] Leclerc H, Périé J-N, Roux S, Hild F. Voxel-scale digital volume correlation. Exp Mech 2011;51(4):479–90.
[77] Lee Y, Chatziathanasiou T, Breite C, Mehdikhani M, Swolfs Y, Mavrogordato MN, Sinclair I, Spearing SM. Cross-resolution benchmarking of digital volume correlation for strain mapping around fibre breaks using in situ synchrotron tomography and holotomography, manuscript currently under review in composites science and technology. 2026.
[78] Lee Y, Chatziathanasiou T, Breite C, Mehdikhani M, Swolfs Y, Mavrogordato MN, Spearing SM, Sinclair I. Correlating fibre break development with fibre misalignment and resin-rich pockets using in situ holotomography. Compos Appl Sci Manuf 2025:109361.
[79] CT datasets for 3D strain mapping around fibre breaks using digital volume correlation. Zenodo; 2026. https://zenodo.org/records/18959885.